China Geology 9 (2026) 25−43

China Geology

Journal homepage: http://chinageology.cgs.cn
https://www.sciencedirect.com/journal/china-geology

Phase field model of fracture propagation and pressure evolution induced by fluid injection considering the effect of initial stress field in power generation test project of Gonghe Basin, China

Hong-wei Wang[a, b, c, d], Hai-dong Wu[a, i,*], He-juan Liu[e, f], Yong-bo Tie[d, g, h], Li-sha Hu[a], Lin-you Zhang[a], Xian-peng Jin[a]

[a] *Center for Hydrogeology and Environmental Geology Survey*, *China Geological Survey*, *Ministry of Natural Resources*, *Tianjin* 300304, *China*
[b] *Chinese Academy of Geological Sciences*, *Ministry of Natural Resources*, *Beijing* 100037, *China*
[c] *Faculty of Engineering*, *China University of Geosciences*, *Wuhan* 430074, *China*
[d] *Chengdu Center of China Geological Survey(Geosciences Innovation Center of Southwest China)*, *Ministry of Natural Resources*, *Chengdu* 610081, *China*
[e] *State Key Laboratory of Geomechanics and Geotechnical Engineering*, *Institute of Rock and Soil Mechanics*, *Chinese Academy of Sciences*, *Wuhan* 430071, *China*
[f] *University of Chinese Academy of Sciences*, *Beijing* 100049, *China*
[g] *Technology innovation center for risk prevention and mitigation of geohazard*, *Ministry of Natural Resources Chengdu* 611734, *China*
[h] *Observation and Research Station of Chengdu Geological Hazards*, *Ministry of Natural Resources*, *Chengdu* 610000, *China*
[i] *Energy and Geoscience Institute*, *University of Utah*, *Salt Lake City*, *UT* 84108, *USA*

A R T I C L E I N F O

Article history:
Received 8 March 2024
Received in revised form 7 September 2024
Accepted 25 September 2024
Available online 17 February 2025

Keywords:
Hot dry rock permeability
Enhance geothermal system (EGS)
Hydraulic stimulation
Phase field model
Fracture propagation
Breakdown pressure
Power generation test
Clean energy geological survey engineering

A B S T R A C T

Hydraulic stimulation technology is widely employed to enhance the permeability of geothermal reservoirs. Nevertheless, accurately predicting hydraulic fracture propagation in complex geological conditions remains challenging, thereby hindering the effective utilization of existing natural fractures. In this study, a phase field model was developed utilizing the finite element method to examine the influence of fluid presence, stress conditions, and natural fractures on the initiation and propagation of hydraulic fractures. The model employs Biot's poroelasticity theory to establish the coupling between the displacement field and the fluid field, while the phase field theory is applied to simulate fracture behavior. The results show that when $\sigma_{x0}/\sigma_{y0} < 3$ or $q_f < 20$ kg/(m^3·s), the presence of natural fractures can alter the original propagation direction of hydraulic fractures. Conversely, in the absence of these conditions, the propagation path of natural fractures is predominantly influenced by the initial stress field. Furthermore, based on the analysis of breakdown pressure and damage area, the optimal intersection angle between natural fractures and hydraulic fractures is determined to range from 45° to 60°. Finally, once a dominant channel forms, initiating and propagating hydraulic fractures in other directions becomes increasingly difficult, even in highly fractured areas. This method tackles the challenges of initiating and propagating hydraulic fractures in complex geological conditions, providing a theoretical basis for optimizing Enhanced Geothermal System (EGS) projects.

©2026 China Geology Editorial Office.

1. Introduction

Geothermal energy represents a significant clean energy source, distinguished by its high stability, renewability, extensive distribution, and substantial reserves (Liu HJ et al., 2015, 2022; Yan XC et al., 2024; Zhang W et al., 2024). Due to the extremely low permeability of rocks in deep geothermal reservoirs, the implementation of permeability enhancement techniques is crucial for facilitating efficient fluid circulation between injection and production wells (Kumari WGP et al., 2019; Li S et al., 2022). Hydraulic fracturing technology represents an efficacious method for stimulating hot dry rock (HDR) reservoirs (Brown et al., 1999). Through the continuous injection of fracturing fluid, fractures progressively expand in length, width, and height, thereby facilitating the interconnection of an increasing number of natural fractures and augmenting the heat exchange surface

First author: *E-mail address*: 291646098@qq.com (Hong-wei Wang).

* Corresponding author: *E-mail address*: wuhaidong@mail.cgs.gov.cn (Hai-dong Wu).

Literary editor: Li-qiong Jia
doi:10.31035/cg2024034
2096-5192/© 2026 China Geology Editorial Office.

Copyright © 2026 Editorial Office of China Geology. Publishing services by Elsevier B.V. on behalf of KeAi Communications Co. Ltd.
This is an open access article under the CC BY-NC-ND License (http://creativecommons.org/licenses/by-nc-nd/4.0/).

area of the HDR reservoir. This process of hydraulic fracturing confers significant economic benefits by enabling the extraction of substantial quantities of resources that were previously deemed inaccessible (Zhou SW et al., 2019).

Numerical simulation has emerged as a viable alternative for investigating hydraulic fracturing, primarily due to the high costs associated with experimental methods, the inherent complexity of reservoirs, and the challenges posed by the invisibility of the fracturing process (Zhou SW et al., 2018a). In addition, engineering disciplines including energy, mechanical, and environmental studies, have increasingly focused on the propagation of fractures within porous media (Mikelic A et al., 2013). During the hydraulic fracturing process, the inadvertent creation of additional channels can lead to risks such as fracturing fluid leakage and disconnection between wells. For instance, the Rosemanowes project determined that higher pressures resulted in fracture growth and greater water loss (Pollack A et al., 2020), and during the 2010 exploitation, tracing tests in the Soultz project exhibited extremely poor connectivity of the GPK–3 and GPK–4 well (Genter A et al., 2013). Thus, hydraulic stimulation relies on the ability to predict fracture propagation paths in porous media. To this end, numerical simulation tools and mathematical models must be developed considering the pre-fracture influences on hydraulic fracture propagation. In particular, hydraulic-mechanical coupling and elastic energy govern fracture propagation in porous media (Yang Y et al., 2017; Zhou SW et al., 2019).

To date, the fractures in solids have been modelled using various discrete, continuous, and hybrid methods. Discontinuities are introduced into the displacement field to implement the discrete approach. In this aspect, the extended finite element method (XFEM) is a common discrete approach that employs remeshing techniques (Moës N et al., 2002; Chen L et al., 2012), element-erosion method (Belytschko T et al., 1987), cohesive element method (Nguyen O et al., 2001; Zhou F et al., 2004) or phantom-node method (Song JH et al., 2006; Rabczuk T et al., 2008; Chau-Dinh T et al., 2012). Additionally, the typical approaches to the mesh-free method include immersed particle method (Rabczuk T et al., 2010a) and cracking-particle method (Rabczuk T et al., 2004, 2010b). In addition to the aforementioned methods, other discrete methods exist, such as discrete element method (DEM) (Shimizu H et al., 2011) and discontinuous deformation analysis (DDA) (Jiao XY et al., 2015). The calculation domain in DDA and DEM is discretized into blocks or particles. The formation of a fracture indicates the elimination of the bonds between the blocks or particles. Moreover, the calibration of the material parameters is extremely complex and the fracture paths are not random.

Compared with the discrete approaches, the continuous approaches such as screened-Poisson models (Areias P et al., 2018) and gradient damage models (Peerlings R et al., 1996) are easier to implement and do not require complex fracture-tracking algorithms. As such, the PFM is a typical continuous method (Miehe C et al., 2010) that was first proposed by Bourdin B et al. (2008). Although hybrid approaches combine the advantages of discrete and continuous approaches and are more effective than discrete approaches, they fail to address the intrinsic drawbacks of discrete approaches (Zhou SW et al., 2019). The common hybrid methods include the finite discrete element method (Yan C et al., 2016) and the DDA-FEM (FEM/DDA) (Choo LQ et al., 2016).

The application of discrete, continuous, and hybrid approaches to hydraulic fracturing has been successful in several cases. For instance, Shimizu H et al. (2011) applied the flow-coupling DEM code to simulate hydraulic fracturing in competent rock. Choo LQ et al. (2016) demonstrated the feasibility of their method for modeling hydraulic fracturing by coupling DDA blocks with finite element meshes. Lecampion B et al. (2009) applied XFEM to resolve the problem of hydraulic fractures. However, predicting the complex fracture interactions in hydraulic fracturing persists to be a challenging task. To this end, phase-field models (PFMs) can be highly effective in solving such problems as it can be applied to coupling issues.

Over the past decade, researchers have achieved remarkable progress in developing accurate and efficient PFMs (Wheeler MF et al., 2014; Miehe C et al., 2015; Santillán D et al., 2017; Li K et al., 2019; Zhuang X et al., 2022). The PFMs and porous medium models based on Biot poroelasticity theory can determine fracture behavior (Zhou SW et al., 2018b). In terms of the energy functional, Wheeler MF et al. (2014) introduced a poroelastic term to the PFM of porous media. Miehe C et al. (2015) proposed a saddle-point principle for Darcy-Biot-type fluid transport at fractures in porous media. Furthermore, Mikelić A et al. (2015) modified the energy functional to decouple the displacement and phase-field problems. Santillán D et al. (2017) employed the PFM method to fully couple the fluid flow in the fracture with the surrounding medium deformation, wherein the fracture was expressed as a diffuse interface. Zhou SW et al. (2018c) proposed a PFM that reproduced the fracture propagation behaviour of porous elastic media. In addition, Li K et al. (2019) developed a total energy functional to explore the propagation of a multizone hydraulic fracture in poroelastic media. Liu J et al. (2020) proposed a mixed PFM to analyse the layered shale fracture behavior in the pre-fractures. Zhuang X et al. (2022) summarized the theoretical and computer implementation of PFMs for fracture characterization. Despite such extensive efforts, recently developed approaches to PFMs in porous media seldom consider the impact of complex nature fractures on fracture propagation.

This research utilized the PFM to investigate the propagation of hydraulic fractures within poroelastic media. Initially, the Biot poroelasticity theory was employed to formulate the coupling between the displacement and fluid fields, while the phase field theory was applied to simulate fracture behavior. Furthermore, the governing equations were derived by incorporating an energy functional fluid. Interpolation functions were then used to modulate the fluid properties between intact and fully fractured media through the phase field. The feasibility and accuracy of the model

were validated prior to analyzing the effects of pre-existing fractures on fracture propagation. The paper is structured as follows: Section 2 presents the mathematical model of dynamic fractures, and section 3 validates the accuracy of the model through comparison with a model case. In section 4, the numerical simulation results are presented to analyze the influence of the Biot coefficient, fluid injection rates, stress distribution, effect of fracture angle, injection point position, and length of natural fracture on the propagation of hydraulic fractures, and the interaction of dynamic hydraulic fracturing with complex natural fractures is illustrated in section 5. Finally, the conclusions of the paper are summarized in section 6.

2. Mathematical model

2.1. Energy functional

When studying the problem of fracture diffusion in pore elastic media, the model is divided into a poro-elastic domain $\Omega \subset \mathrm{R}^{\mathrm{d}}(\mathrm{d}\varepsilon\{2,\ 3\})$ and an internal discontinuity boundary Γ (Fig.1). Brittle fracture theory assumes that the pore size is smaller than the intrinsic length size of the phase field and that the poroelastic domain is homogeneous, isotropic and elastic. The fluid flow in the fracture is viscous and compressible.

In this case, the displacement of body Ω is denoted by $\mathrm{u}(x,\mathrm{t}) \subset \mathrm{R}^{\mathrm{d}}$ at time $\mathrm{t} \in [0,\mathrm{T}]$, x is the position vector and the computational time interval $\mathrm{T} > 0$. The Dirichlet boundary conditions depend on time in the displacement field, $\mathrm{u_i}(x,\mathrm{t}) = \mathrm{g_i}(x,\mathrm{t})$, on $\partial\Omega_{\mathrm{gi}} \in \Omega$, and the Neumann conditions are time-dependent, $\partial\Omega_{\mathrm{hi}} \in \Omega$. The traction $\mathrm{f}(x,\mathrm{t})$ acts on the boundary $\partial\Omega_{\mathrm{hi}}$, and Ω is subjected to a body force $\mathrm{b}(x,\mathrm{t}) \subset \mathrm{R}^{\mathrm{d}}$.

The initial fluid pressure field p_0, displacement field u_0 and stress field σ_0 of the porous domain are known in advance. On the other hand, after passing through hydraulic fracturing, the fluid pressure, stress and displacement are $p_0 + p$, σ and $u_0 + u$, respectively. It should be noted that u_0 represents the displacement change induced by underground engineering, whereas the displacement due to long-term *in-situ* stress is neglected (Zhou SW et al., 2020a). Based on Griffith's theory, the critical energy release rate equals the critical fracture energy density G_{c}, that is, the energy producing the fracture surface per unit area (Francfort GA et al., 1998). For a single-phasic solid ψ, the energy functional is defined as the fracture energy ψ_{f}, the elastic energy $\psi_\varepsilon(\varepsilon)$, and the work from external forces W_{ext} (Eq. 1). However, for the extension of fractures in porous elastic materials by pressure and fluid-driven, the effect *of pressure* p should be considered in the energy function (Lee S et al., 2016; Zhou SW et al., 2020b).

$$\Psi(\mathbf{u},p,\Gamma) = \underbrace{\int_{\Omega\backslash\Gamma}\psi_\varepsilon(\varepsilon)d\Omega}_{\Psi_\varepsilon} - \underbrace{\int_{\Omega}\alpha p\cdot(\nabla\cdot\mathbf{u})d\Omega}_{pressure-related\ term} - \underbrace{\int_{\Gamma}G_C d\Gamma}_{\Psi_f} - \underbrace{\int_{\partial\Omega\Gamma}f_t\mathbf{u}dS}_{W_{ext}} \tag{1}$$

where $\psi_\varepsilon(\varepsilon)$ is the elastic energy density and G_c is the critical energy release rate; $\alpha \in (0\,,1]$ is the Biot coefficient; f_t represents the traction at the Neumann boundary in dS. The linear strain tensor $\varepsilon_{\mathrm{ij}}$ can also be expressed as (Eq. 2):

$$\varepsilon_{ij} = \frac{1}{2}\left(\frac{\partial u_i}{\partial x_j} + \frac{\partial u_j}{\partial x_i}\right) \tag{2}$$

$\psi_\varepsilon(\varepsilon)$ is the elastic energy density, if the heterogeneity of the model is not considered, it can be defined as (Miehe C et al., 2010; Eq. 3):

$$\psi_\varepsilon(\varepsilon) = \frac{1}{2}\lambda\varepsilon_{ii}\varepsilon_{jj} + \mu\varepsilon_{ij}\varepsilon_{ij} \tag{3}$$

where the Lamé constants λ,μ can be written as (Eq. 4):

$$\begin{cases} \lambda = \dfrac{E\nu}{(1+\nu)(1-2\nu)} \\ \mu = \dfrac{E}{2(1+\nu)} \end{cases} \tag{4}$$

With $\lambda,\mu > 0$, E and ν are the Young's modulus and Poisson's ratio, respectively.

Considering the influence of the initial stress field, the energy equation can be expressed as (Shiozawa S et al., 2019; Zhou SW et al., 2020a; Eq. 5):

$$L(\mathbf{u},p,\Gamma) = \underbrace{\int_{\Omega\backslash\Gamma}\psi_\varepsilon(\varepsilon)d\Omega}_{\psi_\varepsilon} + \underbrace{\int_{\Omega\backslash\Gamma}\sigma_0 : \varepsilon d\Omega}_{initial\ stress\ induced} - \underbrace{\int_{\Omega}\alpha p\cdot(\nabla\cdot\mathbf{u})d\Omega}_{pressure-related\ term} + \underbrace{\int_{\Gamma}G_C d\Gamma}_{\psi_f} - \underbrace{\int_{\partial\Omega\backslash\Gamma}f_t\mathbf{u}dS}_{W_{ext}} \tag{5}$$

2.2. Phase field description

The PFM enables graceful simulation of complex

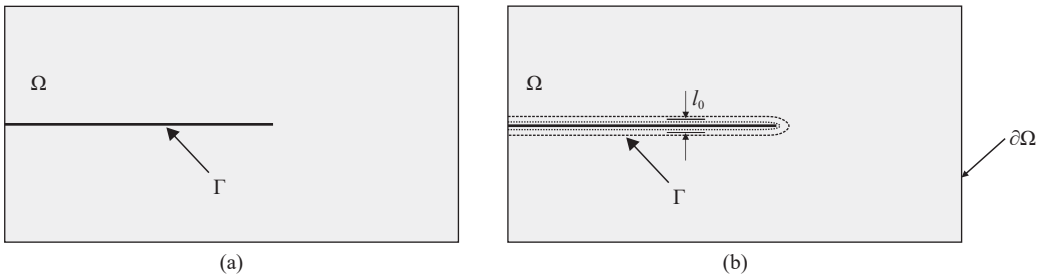

Fig. 1. Sharp and diffusive fracture in the solid Ω. a–Sharp fracture surface Γ, and b–diffusive fracture.

breaking processes using only a scalar field including fracture initiation, propagation, coalescence, and branching (Zhuang X et al., 2022). To simplify the numerical implementation and avoid complex crack tracking procedures, fracture surface Γ can be expressed using a phase field $\phi(x,t) \in [0,1]$ (Li K et al., 2019; Zhou SW et al., 2020b). Where $\phi = 1$ denotes the rock 'fully' broken rock while $\phi = 0$ indicates the intact rock. When the phase field $\phi(x,t) \in (0,1)$ indicates that the rock is in an transition region (Eq. 6). In phase fields, the fracture surface density per unit volume is represented by gradients (Bourdin B et al., 2000; Miehe C et al., 2010).

$$\gamma(\phi, \nabla\phi) = \frac{\phi^2}{2l_0} + \frac{l_0}{2}\frac{\partial\phi}{\partial x_i}\frac{\partial\phi}{\partial x_i} \tag{6}$$

where l_0 is the length scale parameter. It is important to note that l_0 limits the transition area between unbroken areas and fully cracked. In addition, it can also be viewed as a parameter of material strength. In the phase-field model, the nominal tensile strength of the material decreases when the l_0 value is large (Borden MJ et al., 2012; Zhou SW et al., 2018b). When the pore size of the domain is much smaller than its length scale, the fracture energy is given as (Eq. 7):

$$\Psi_f = \int_\Gamma G_C dS \approx \int_\Omega G_C \gamma d\Omega = \int_\Omega G_C \left(\frac{\phi^2}{2l_0} + \frac{l_0}{2}\frac{\partial\phi}{\partial x_i}\frac{\partial\phi}{\partial x_i}\right) d\Omega \tag{7}$$

where G_c is the isotropic energy release rate. Elastic energy is divided into compressive and tensile components (Miehe C et al., 2010; Eq. 8).

$$\varepsilon_\pm = \sum_{a=1}^{d} \langle\varepsilon_a\rangle_\pm \mathbf{n}_a \otimes \mathbf{n}_a \tag{8}$$

where ε_+ is the tensile strain tensors, ε_- is the compressive strain tensors, $<\varepsilon_a>_\pm = (\varepsilon_a \pm |\varepsilon_a|)/2$, $\boldsymbol{n}_a$ and ε_a are its direction and the principal strain. The stretched and compression parts after elastic energy density decomposition are expressed as (Eq. 9):

$$\psi_\varepsilon^\pm(\varepsilon) = \frac{\lambda}{2}\langle tr(\varepsilon)\rangle_\pm^2 + \mu tr\left(\varepsilon_\pm^2\right) \tag{9}$$

Assuming that the extension of the crack is not affected by the elastic energy density of the compressed component, the elastic energy can be written as follows (Borden MJ et al., 2012; Eq. 10):

$$\psi_\varepsilon = \int_{\Omega\backslash\Gamma} \psi_\varepsilon(\varepsilon) d\Omega = \int_\Omega \left[g(\varphi)\psi_\varepsilon^+(\varepsilon) + \psi_\varepsilon^-(\varepsilon)\right] d\Omega \tag{10}$$

The degradation function $g(\varphi)$ satisfies $g(0) = 1$, $g(1) = 0$, $g'(1) = 0$ (Ambati M et al., 2015). The quadratic form of the $g(\varphi)$ is $g(\varphi) = (1-k)(1-\varphi)^2 + k$.

The degradation function considering the energy change caused by the initial stress can be described as follows (Eq. 11):

$$\int_{\Omega\backslash\Gamma} \sigma_0 : \varepsilon d\Omega \approx \int_\Omega g(\varphi)\sigma_0 : \varepsilon d\Omega \tag{11}$$

2.3. Displacement description

Combined with the above equations, the energy function can be rewritten as follows (Eq. 12):

$$\begin{aligned} L = &\int_\Omega \left[g(\phi)\psi_\varepsilon^+(\varepsilon) + \psi_\varepsilon^-(\varepsilon)\right] d\Omega + \int_\Omega g(\phi)\sigma_0 : \varepsilon d\Omega - \\ &\int_\Omega \alpha p \cdot (\nabla \cdot \mathbf{u}) d\Omega + \int_\Omega G_C \left[\frac{\phi^2}{2l_0} + \frac{l_0}{2}\nabla\phi \cdot \nabla\phi\right] d\Omega - \\ &\int_{\partial\Omega h} f_t \cdot \mathbf{u} dS \end{aligned} \tag{12}$$

When the energy functional L is 0 in the first variation, yielding (Francfort GA et al., 1998; Eq. 13)

$$\begin{aligned} \delta L = &\int_{\partial\Omega h} \underbrace{\left[\left(\sigma_{ij}^e + g(\phi)\sigma_{oij} - \alpha p\delta_{ij}\right) m_j - f_{ti}\right] \delta u dS}_{a} - \\ &\int_\Omega \underbrace{\left(\sigma_{ij}^e + g(\phi)\sigma_{oij} - \alpha p\delta_{ij}\right) \delta u_i d\Omega}_{b} - \\ &\int_\Omega \underbrace{\left[g'(\phi)\left(\psi_\varepsilon^+ + \sigma_{oij}\varepsilon_{ij}\right) + \frac{G_C\phi}{l_0} - G_C l_0 \frac{\partial^2\phi}{\partial x_i^2}\right] \delta\phi d\Omega}_{c} + \\ &\int_{\partial\Omega} \underbrace{\left(\frac{\partial\phi}{\partial x_i} m_i\right) \delta\phi dS}_{d} = 0 \end{aligned} \tag{13}$$

where $g'(\phi) = dg(\phi)/d\phi = 2(\phi-1)(1-k)$ and m_j is the normal vector of the boundary. The effective stress tensor is determined by component σ_{ij}^e and variable $\sigma(\varepsilon)^e$ is induced by the displacement u (Eq. 14):

$$\begin{aligned} \sigma^e = &g(\phi)\frac{\partial\psi_\varepsilon^+}{\partial\varepsilon} + \frac{\partial\psi_\varepsilon^-}{\partial\varepsilon} = [(1-k)(1-\phi)^2 + k] \\ &[\lambda\langle tr(\varepsilon)\rangle_+ I + 2\mu\varepsilon_+] + \lambda\langle \mathrm{tr}(\varepsilon)\rangle_- I + 2\mu\varepsilon_- \end{aligned} \tag{14}$$

where $I \in R^{d\times d}$ is the identity tensor.

The total stress tensor σ can be written as (Eq. 15):

$$\sigma(\varepsilon) = \sigma^e(\varepsilon) + g(\phi)\sigma_0 + \alpha pI, \text{in } \Omega \times (0,T] \tag{15}$$

where δ_u must satisfy Eq. 13, and based on the Dirichlet and Neumann boundary conditions (Zhou SW et al., 2020a; Eq. 16).

$$\sigma_{ij} m_j = f_{ti}, on\ \partial\Omega_h \times (0,T] \tag{16}$$

Eq. 13[b] gives rise to the governing equation (Eq. 17):

$$\frac{\partial\sigma_{ij}}{\partial x_j} = 0, in\ \Omega \times (0,T] \tag{17}$$

2.4. Phase field equations

As a result, Eq. 18 indicates the driving mechanism for fracture initiation and propagation:

$$\left[\frac{2l_0(1-k)H}{G_C} + 1\right]\phi - l_0^2\frac{\partial^2\phi}{\partial x_i^2} = \frac{2l_0(1-k)H}{G_C}, in\ \Omega \times (0,T] \tag{18}$$

In order to form a phase field that monotonically increases, a history reference field H is required (Eq. 19):

$$H(\boldsymbol{x},t)=\max_{s\in[0,t]}\left[\psi_{\varepsilon}^{+}(\boldsymbol{\varepsilon}(\boldsymbol{x},s))+\boldsymbol{\sigma}_0:\boldsymbol{\varepsilon}(\boldsymbol{x},s)\right],\text{in }\Omega\times(0,\mathrm{T}] \quad (19)$$

It meets the Neumann condition (Eq. 20):

$$\frac{\partial\phi}{\partial x_i}m_i=0, on\ \partial\Omega\times(0,\mathrm{T}] \quad (20)$$

As a result, Eq. 19 indicates that $H(x,t)$ drives fracture initiation and propagation.

2.5. Equations for the fluid flow

Domain Ω is divided into three segments: fracture domain $\Omega_f(t)$, transition domain $\Omega_t(t)$ and unbroken domain $\Omega_r(t)$. Two thresholds c_1 and c_2 were used to distinguish between the three domains (Lee S et al., 2016). When $\phi\geqslant c_2$, material can be treated as $\Omega_f(t)$, when $\phi\leqslant c_1$ as matrix domain $\Omega_r(t)$, and transition domain $\Omega_t(t)$ at $c_1<\phi<c_2$. Two linear indicator functions (χ_r and χ_f) are defined to connect the $\Omega_t(t)$ with $\Omega_r(t)$ and $\Omega_f(t)$. The indicator function $\chi_r=1$ in the reservoir domain and $\chi_r=0$ in the fractured domain. In contrast, $\chi_f=0$ in the reservoir domain and $\chi_f=1$ in the fractured domain (Shiozawa S et al., 2019; Fig. 2). In addition, the indicator functions satisfy the following (Lee S et al., 2016; Li K et al., 2019; Eq. 21):

$$\begin{cases}\chi_r(\cdot,\phi)=\dfrac{c_2-\phi}{c_2-c_1} & c_1<\phi<c_2\\ \chi_f(\cdot,\phi)=\dfrac{\phi-c_1}{c_2-c_1} & c_1<\phi<c_2\end{cases} \quad (21)$$

Fluid flow in the pore elastic medium follows Darcy's law, mass conservation equation as follows (Zhou SW et al., 2018b; Eq. 22):

$$\rho S\frac{\partial p}{\partial t}-\nabla\cdot\frac{\rho K_{eff}}{\mu_{eff}}\left(\nabla p+\rho g\right)=q_m-\rho\alpha\chi_r\frac{\partial\varepsilon_{vol}}{\partial t} \quad (22)$$

where ρ is the density of fluid (kg/m^3), $K_{eff}=K_r\chi_r+K_f\chi_f$ is the effective permeability and fluid viscosity is calculated by $\mu_{eff}=\mu_r\chi_r+\mu_f\chi_f$. q_m is source term (kg/m^3/s). α is the Biot coefficient. In Eq. 22, $\rho=\rho_r\chi_r+\rho_f\chi_f$ and $\alpha=\alpha_r\chi_r+\alpha_f\chi_f$ where symbol "r" indicates parameters in the rock matrix and symbol "f" indicates parameters in the fracture. In addtition, S is storage coefficient (1/Pa), expressed as:

$$S=\varepsilon_p c+\frac{(\alpha-\varepsilon_p)(1-\alpha)}{K_{Vr}} \quad (23)$$

where ε_p is porosity, c is fluid compressibility (1/Pa) and K_{Vr} is bulk modulus of the calculation domain (Pa). Similarly, $c=c_r\chi_r+c_f\chi_f$, where c_f and c_r as the fluid compressibility in the fractured and reservoir domains.

The Neumann boundary condition on $\partial\Omega_N$ and the Dirichlet boundary condition on $\partial\Omega_D$ are given by (Zhou SW et al., 2020a; Eq. 24):

$$\begin{cases}p=p_D & on\quad\partial\Omega_D\\ -\mathbf{n}\cdot\rho\mathbf{v}=M_N & on\quad\partial\Omega_N\end{cases} \quad (24)$$

where p_D is the prescribed pressure while M_N is the prescribed mass flux.

2.6. Numerical simulation implementation

Finite element method (FEM) is used to solve the governing equation for multi-field fracture problems in porous mediums. Therefore, a weak form formula (Zhou SW et al., 2018b) and a modified stiffness matrix are needed to solve the displacement field. The implicit generalized α method (Borden MJ et al., 2012) is used to discretize the time domain and improve the numerical stability unconditionally. The authors seek to solve these three fields in a staggered manner (Fig. 3). That is, the three domains are independent of each other when they are solved in a one time step (Zhou SW et al., 2018b, 2019). Where, u and p are combined to solve them in a staggered step. Fig. 4 shows the flowchart of numerical calculation procedures.

3. Verification of the model

3.1. Validation of the model for internal fluid injection

A simple example simulating the fluid-induced fracture expansion at increasing fracture pressure validates the accuracy of the computational algorithm for hydraulic fracturing dynamics problems. Several tests have been performed on Zhuang X et al. (2020) based on this example. The geometry model of the case is shown in Fig. 5. The model size is 90 m×60 m, the prefabricated fracture is located

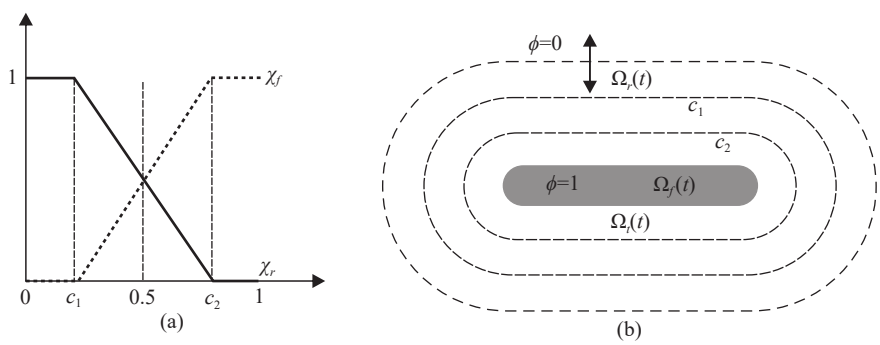

Fig. 2. a–Linear indicator functions χ_r and χ_f; b–the fracture and reservoir domains.

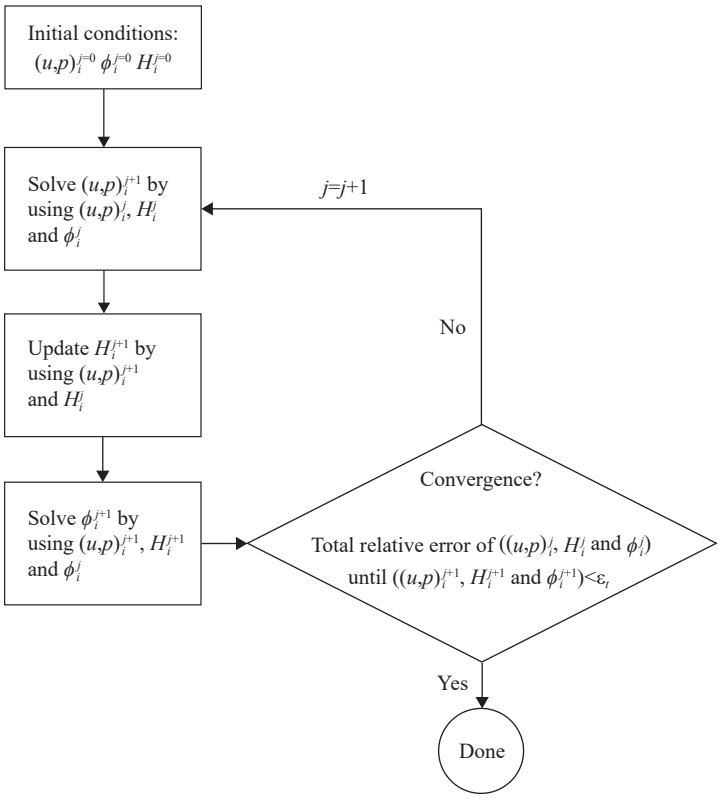

Fig. 3. Staggered scheme flow chart of fracture propagation in porous media.

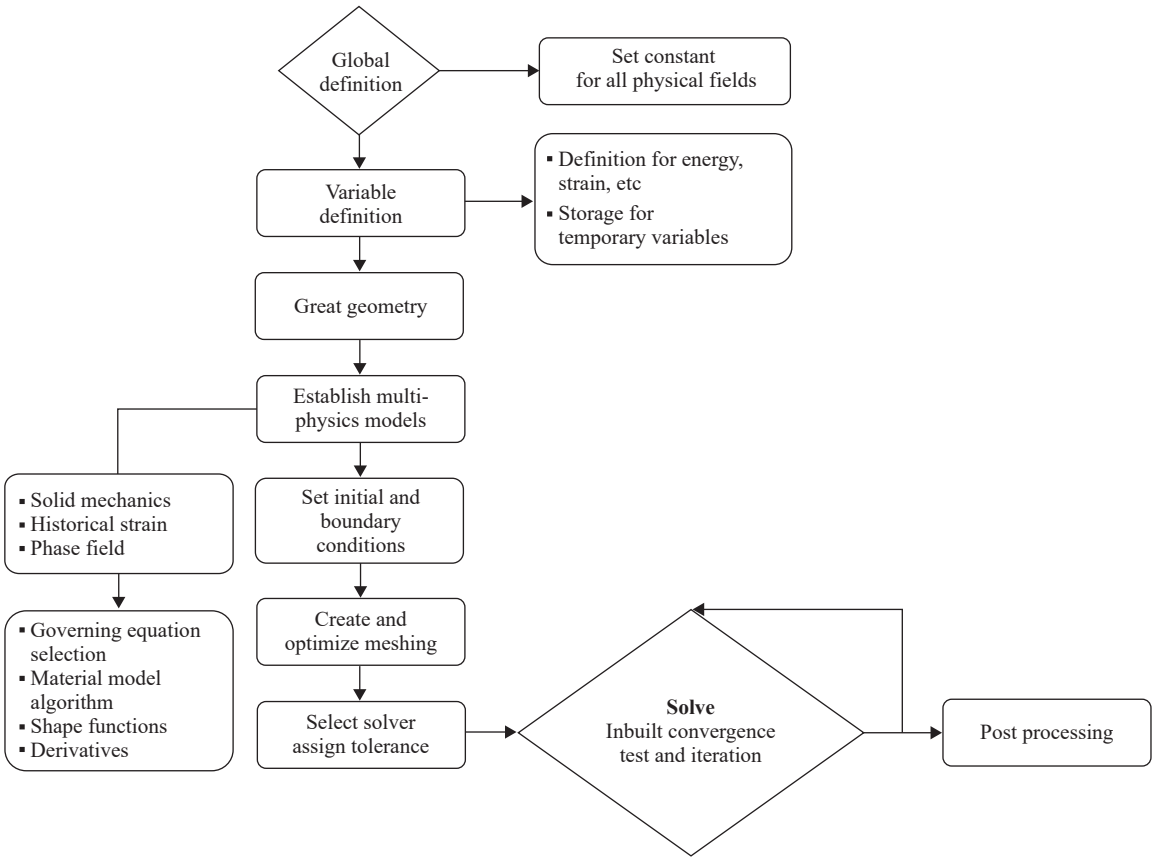

Fig. 4. Flowchart of numerical calculation procedures.

in the middle of the model, and the length is 1.2 m. Fluid pressure of $p_0 = 0$ is applied to all outer boundaries of the calculation domain in order to eliminate the effect of rigid body displacements. The parameters used in the model are

shown in Table 1 and the other conditions refer to Zhuang X et al. (2020).

To improve the efficiency of the model calculation, set the element size of mesh $h = 0.2$ m. The model uses a time-dependent study to calculate the liquid-induced fracture propagation in the case of increased fracture pressure for a total of 1200 time steps with the time increment $\Delta t = 0.025$. Fig. 6 illustrates the fracturing propagation and displacement field varies obtained by using the PFM and taking into account the initial stress field. It shows that the stress does not affect the fracture propagation at $\sigma_{x0} = \sigma_{y0}$, which travels along a horizontal direction. Fig. 7 compares the fluid pressure-time curve calculated by Santillán D et al. (2017) with the numerical solutions. It is similar between the pressure variation curve and the analytical solution (Santillán D et al., 2017). The variance observed in the pressure curve during the initial seconds can be attributed to the fact that the fluid takes some time to load the pressure before reaching the breakdown pressure. Fig. 8 shows the hydraulic fracture length of the model at various times, matching well with previous studies by Santillán D et al. (2017) and Zhuang X et al. (2020). However, the discrepancy in the results may be attributed to unknown software parameters or inconsistent solver configurations.

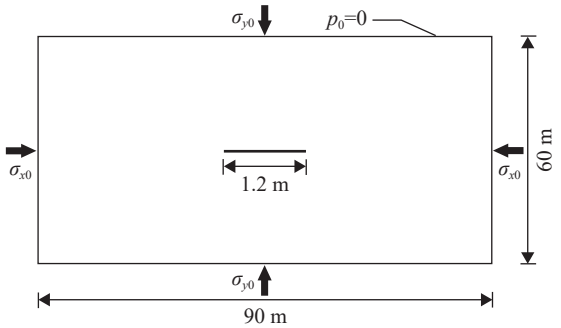

Fig. 5. Geometric model of the calculation domain.

Table 1. Parameters of the verify model (after Zhuang X et al., 2020).

Parameter	Value	Unit	Parameter	Value	Unit
μ	4.722	GPa	λ	7.083	GPa
G_c	120	N/m	k	1×10^{-9}	–
l_0	0.4	m	c_1	0.4	–
c_2	1.0	–	$\varepsilon_p R$	0.088	–
ρ_r, ρ_f	1.0×10^3	kg/m^3	α_r	0.088	–
q_r	0	kg/(m^3·s)	Q_f	10^{-3}	m^2/s
k_r	1×10^{-15}	m^2	k_f	5×10^{-8}	m^2
c_r	1×10^{-8}	1/Pa	c_f	1×10^{-8}	1/Pa
μ_r	1×10^{-3}	Pa·s	μ_f	1×10^{-3}	Pa·s

3.2. Propagation of hydraulic fractures under nature fractures

The effect of natural fractures on the propagation of hydraulic fractures was verified by an example of a pre-existing vertical fracture. The model size is 4 m×4 m, the nature fracture (NF) is vertical hydraulic fracture (HF), and the length is 1 m (Fig. 9). There are a total of 1200 time steps and the time increment Δt = 0.01 s in the model. The parameters of the model are described in Zhou SW et al. (2018b). Fig. 10 displays the fracture propagation results at 6 s, 6.8 s, 8 s and 11.6 s, respectively. Fig. 11 illustrates how the internal pressure of horizontal fractures varies over time. The numerical results are consistent with Zhou SW et al. (2018c).

4. Results and discussion

Fracture is the essential element constituting the fracture network. Therefore, the established HDR reservoirs completely utilize and leverage the natural fractures through a detailed study of practical engineering according to the geological conditions. To increase reservoir conductivity, reduce fracturing cost, and improve fracturing efficiency,

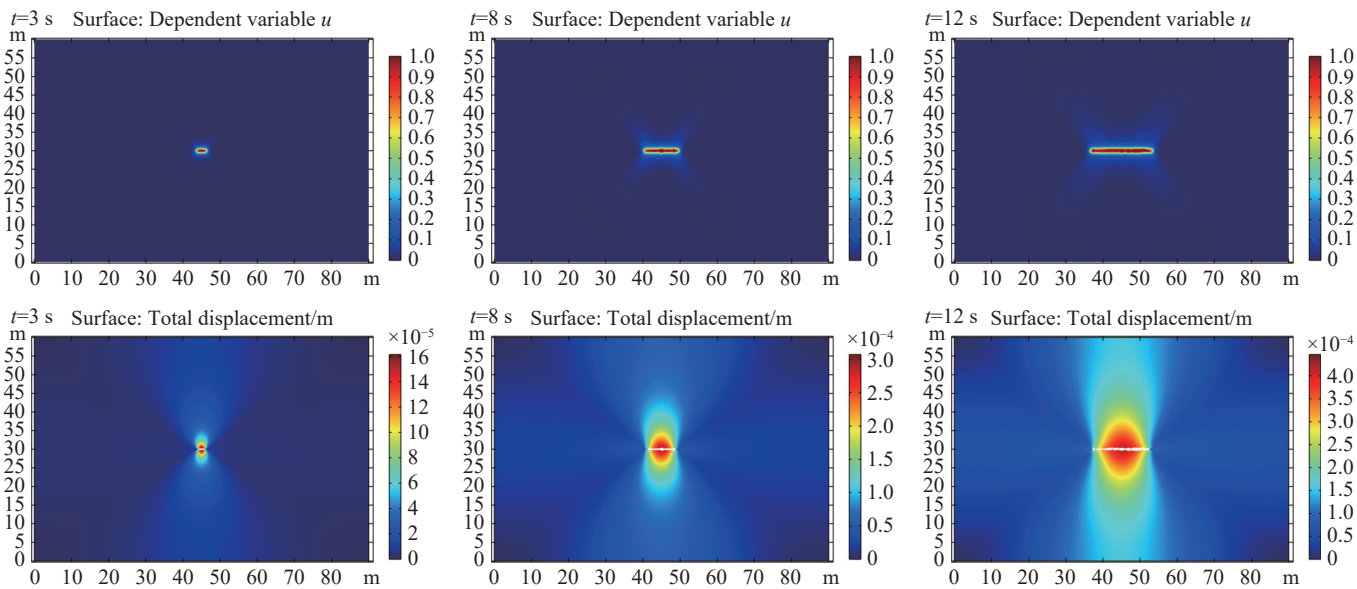

Fig. 6. Horizontal fracture propagation and displacement field varies at different times.

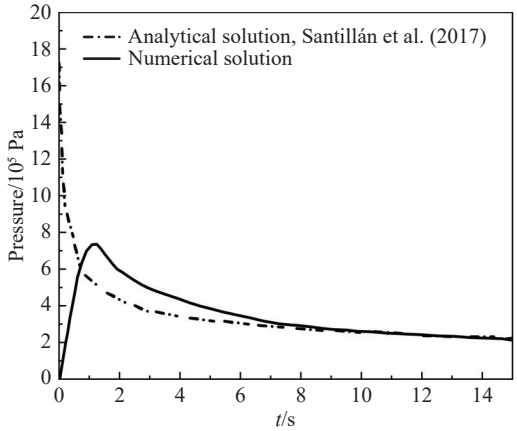

Fig. 7. Hydraulic pressure variation curve for numerical solutions and analytical solution.

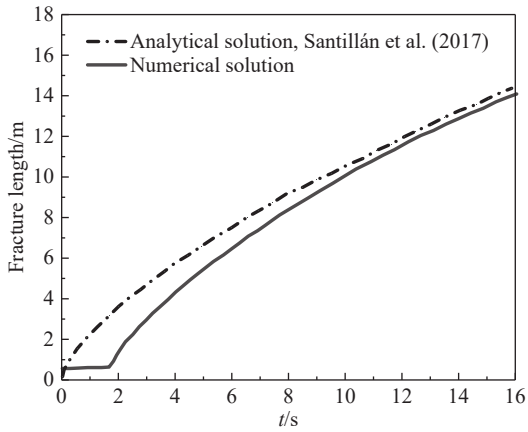

Fig. 8. Hydraulic fracture length of the model.

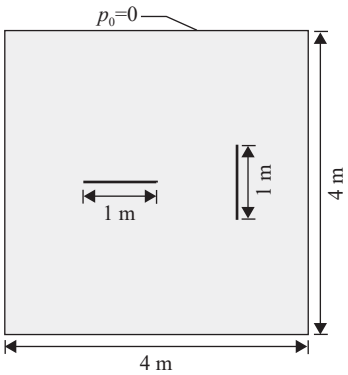

Fig. 9. Geometric model of the two perpendicular pre-existing fractures.

scholars have attempted to predict and control the direction of the fracture propagation and realize the communication between each branch joint by opening and expanding the natural fracture. Therefore, understanding the impact of natural fracture (NF) on the seepage characteristics of the fractured rock mass poses immense theoretical significance and practical application in several fields such as geology and underground energy extraction.

This study set up a series of two-dimensional numerical models of the underground fractured rock mass to investigate the effects of stress variations on fracture propagation and model fluid pressure. As depicted in Fig. 12, it is a single natural fracture model which σ_{x0} and σ_{y0} denote the initial horizontal maximum principal stress and minimum principal stress, respectively. To examine the fracture propagation in presence of a NF, this study formulated a 2D model of fluid injection containing natural fractures with length and width of 30 m and 15 m, respectively. In the COMSOL Multiphysics simulator, the model displayed four distinct intersection angles for the fractures: $\theta = 30°$, 45°, 60°, and 90°. In the fundamental scenario, $\sigma_{x0} = 20$ MPa and $\sigma_{y0} = 10$ MPa. The NFs and artificial prefabricated fractures exhibited a length of 5 m, and the point of hydraulic pressure monitoring is located at the entrance of the fracture.

To eliminate the effect of rigid body displacement, the displacement of the rigid body was set to zero and the fluid pressure of the exterior boundary was set as $p = 0$.

The hot dry rock reservoir located in the Gonghe Basin of Qinghai Province primarily consists of granite and is situated at depths of approximately 4000 m within the heat storage range (Zhang EY et al., 2022). In all examples, the calculation parameters are listed in Table 2 and the source term in the injection position notches is set as $q_f = 10\ \mathrm{kg/(m^3 \cdot s)}$ (Zhou SW et al., 2020a). Domain discretization was performed using free triangular elements with a maximum element size of h = 0.05 m. Furthermore, the simulation employed a time step of $t = 0.2$ s.

4.1. Pressure and the displacement variations

For a homogeneous medium, the shape of hydraulic fractures depends on the mechanical properties of the rock as well as the *in-situ* stress and rheological energy of fracturing fluid. Generally, in homogeneous strata, the hydraulic fractures tend to propagate perpendicular to the direction of the minimum principal stress (Gao Q et al., 2018). Fundamentally, these phenomena were caused by a large principal stress constricting the seepage channel of fluid flow in the opposite direction, which inhibited or suppressed the rate of liquid seepage in that direction, thereby hindering fracture propagation and rock failure. In practical engineering, owing to the existence of natural fractures, the formation conditions will become heterogeneous and the propagation of the fractures will be affected as well (Wang HW et al., 2024). Fig. 13 illustrates the hydraulic pressure response with an existing natural fracture. Initially, the hydraulic fracture develops along the direction of the maximum horizontal principal stress. Thereafter, the hydraulic fracture is encapsulated by the natural fracture at time t = 10 s. Eventually, the natural fractures propagate along the hydraulic fractures and are more easily distributed within the natural fracture because the fluid evolves with less resistance. Finally, after crossing the natural fracture, it continues to evolve in the direction of the maximum principal stress in the matrix.

The displacement profile over time t at $\theta = 45°$ is plotted in Fig. 14. To more clearly reflect the fracture shape of the

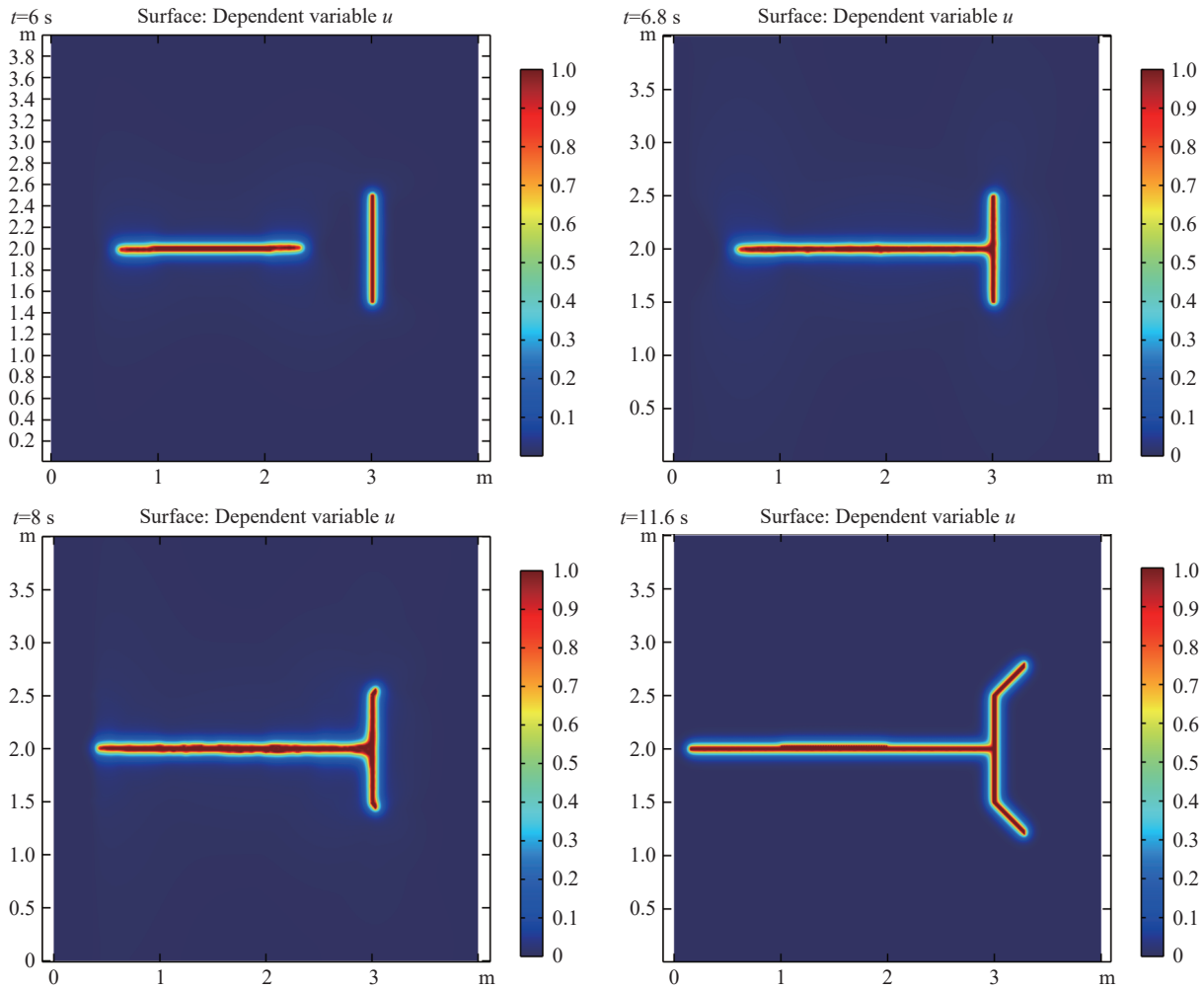

Fig. 10. Propagation of hydraulic fractures under a perpendicular pre-existing fracture.

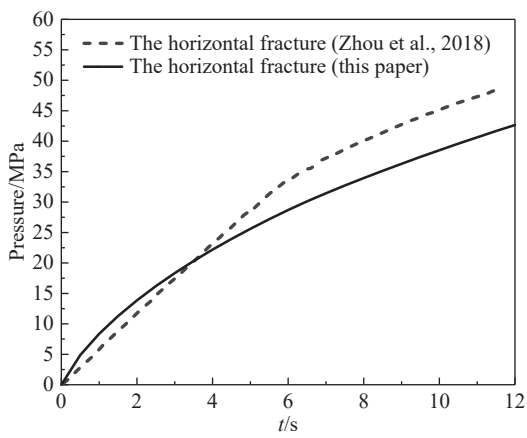

Fig. 11. Comparison of the pressure−time curves under the influence of horizontal natural fractures.

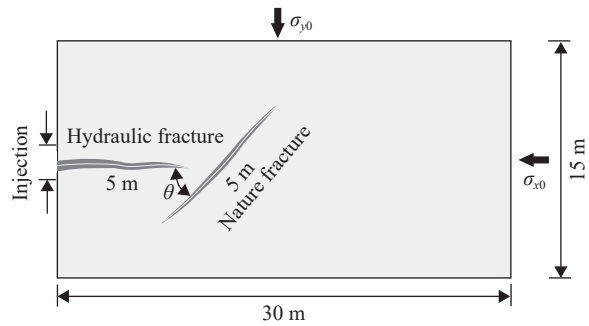

Fig. 12. Nature fracture and hydraulic fracture interference diagram.

displacement field, the displacement deformation is 1000-fold. As observed, the fractures initially propagated in the horizontal direction; however, the direction of propagation varied significantly after encountering the NF.

4.2. Biot coefficients

The classical theory of poroelasticity developed by Biot MA (1941) has applications in geoscience and geomechanics, such as energy resource extraction and transport of environmental pollutants, etc. The Biot coefficient was an important advance of stress distribution in fluid-saturated porous media for hydro-mechanical and thermo-hydro mechanical processes (Selvadurai APS et al., 2021). It solves the problem of partitioning externally applied stresses between porous skeletons and pore fluid. The Biot coefficient, which is determined by the bulk moduli of porous materials and solid materials, can be written as (Selvadurai APS et al., 2020; Wang HW et al., 2022; Eq. 25):

$$\alpha = 1 - \frac{K_D}{K_S} \tag{25}$$

where K_D and K_S are the bulk moduli values for the porous skeleton and the solid material, respectively. Therefore, experiments are required to determine the size of the Biot coefficient and the concepts involved in the experimental procedure are shown in Fig. 15. Notably, in order to ensure the compressibility of solid materials with porous skeletons, the pore space needs to be saturated completely.

For marble and granite, the Biot coefficient is lower than 0.5 (Selvadurai APS et al., 2020). Thus, to study the effect of Biot coefficient on fracture expansion, the Biot coefficients were 0.1, 0.2, 0.3, 0.3, 0.4, and 0.5. The geometric model is shown in Fig. 14 and the parameters are shown in Table 2. Fig.16 shows that the hydraulic pressure variation over time with the different Biot coefficients in the rocks. When $\alpha = 0.1$, after fluid injection, the hydraulic pressure is gradually increased and the pressure does not decrease significantly. This means that rock fracturing has not occurred during this time period. When $\alpha = 0.2$, after 29 s, the pressure curve shows a slight drop, indicating that the rock is likely to reach the breakdown pressure. The reservoir breakdown pressure gradually decreases with the increase in Biot coefficient. Fig. 17 illustrates the effect of the Biot coefficient on the rock damage ratio. The reservoir damage rate increases as the Biot coefficient increases.

Table 2. Model parameters (after Li K et al., 2019; Zhang EY et al., 2022; Lei Q et al., 2021).

Parameter	Value	Parameter	Value	Parameter	Value
E	41.28 GPa	ν	0.27	c_a	1×10^5
l_0	2×10^{-3} m	α_r	0.002	ρ_r	1×10^3 kg/m^3
c_1	0.4	c_2	1.0	ε_{pr}	0.002
c_r	1×10^{-8}1/Pa	c_f	1×10^{-8}1/Pa	μ_r	1×10^{-3}1/Pa·s
c_b	2	k	1×10^{-9}	K_r	1×10^{-15} m^2
ρ_f	1×10^3 kg/m^3	μ_f	1×10^{-3} Pa·s		

4.3. Fluid injection rates

As the shapes of hydraulic fracture propagation in natural fractures can be affected by the fluid injection rates during hydraulic fracturing, the influence of fluid injection rates on hydraulic fracture propagation should be analyzed. To facilitate observation, only the injection rates were altered while maintaining the other parameters unchanged. The angle between the injection unit and natural fracture (90°) did not vary, and the source term in the injection position varied as follows: (1) $q_f = 10$ kg/(m$^3\cdot$s); (2) $q_f = 15$ kg/(m$^3\cdot$s); (3) $q_f = 20$ kg/$\left(\text{m}^3\cdot\text{s}\right)$; (4) $q_f = 25$ kg/$\left(\text{m}^3\cdot\text{s}\right)$. The results are presented in Fig. 18 (fracture aperture is 1000-fold), which indicates low fluid injection rates ensuring the disintegration of the rock, the flow of the hydraulic fractures along the natural fractures, and the opening of the fracture and flowing out of the weak surfaces or tips. Nevertheless, for excessively high injection rates, the hydraulic fractures may pass directly through the natural fractures. Currently, the natural fractures

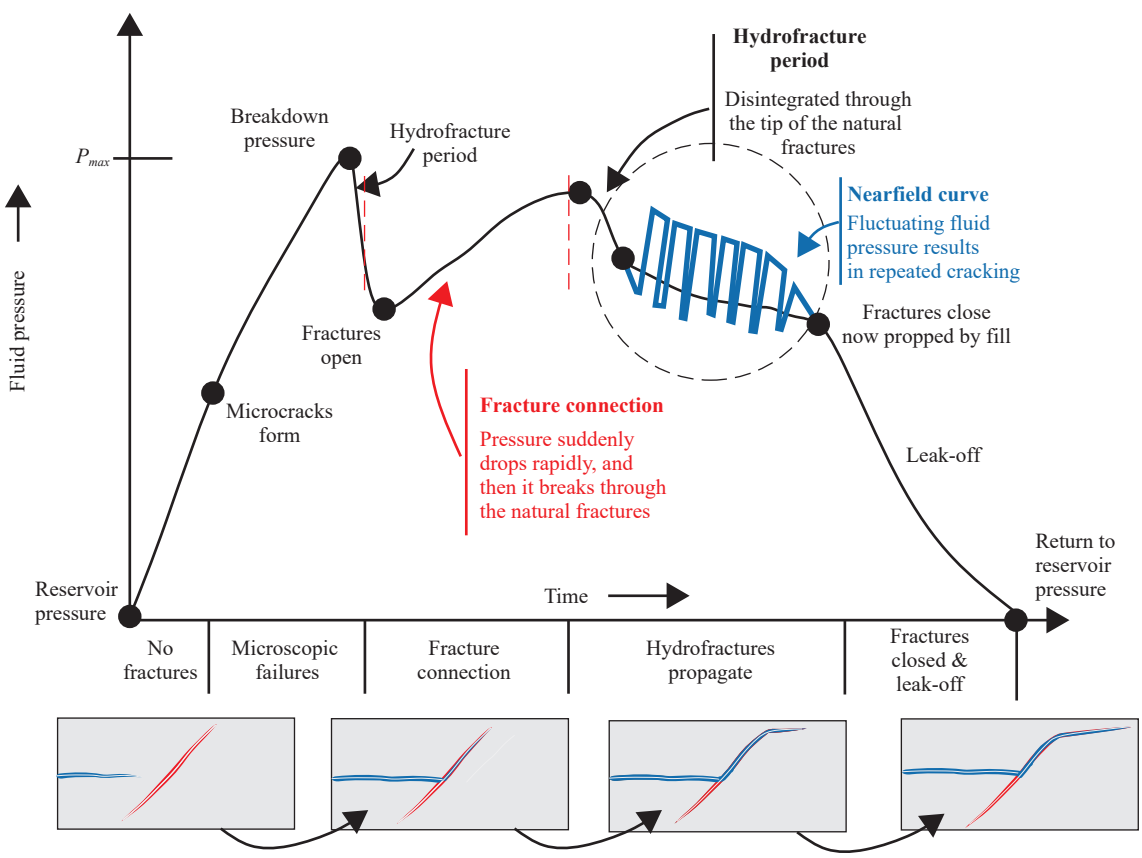

Fig. 13. Hydraulic pressure evolution and hydro fracture propagation with existing natural fracture.

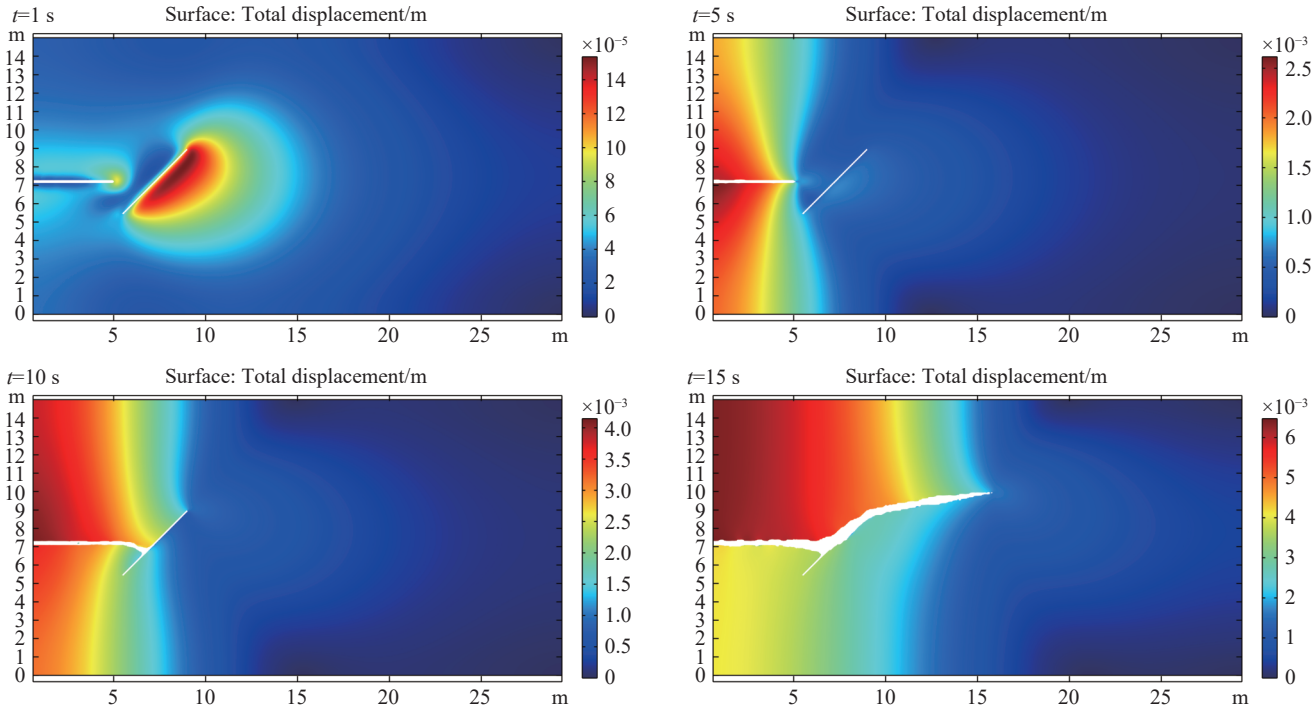

Fig. 14. Displacement profile with respect to time.

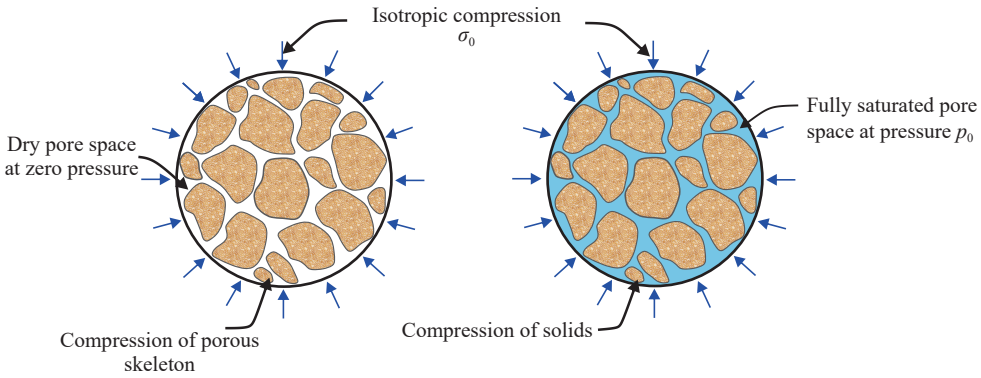

Fig. 15. Experimental configurations for estimating Biot coefficient.

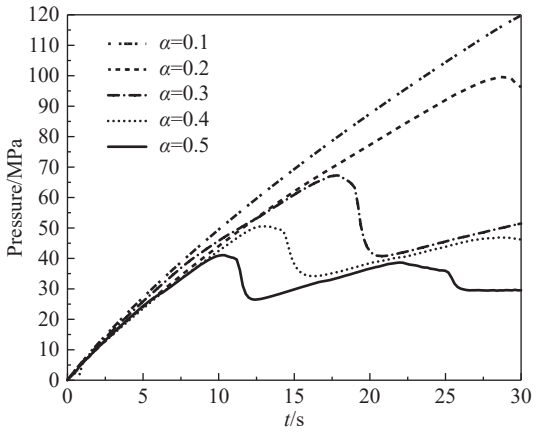

Fig. 16. Hydraulic pressure variation curve over time with various Biot coefficient.

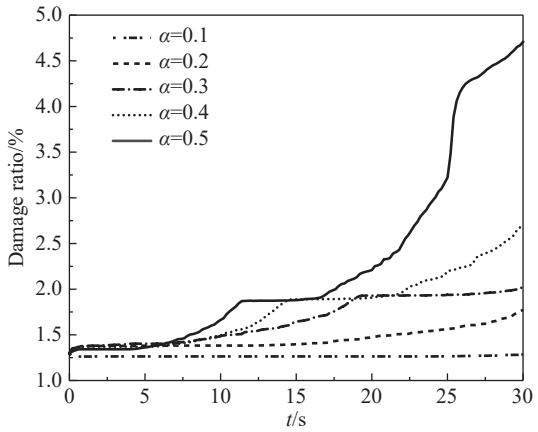

Fig. 17. Rock damage ratio variation curve over time with various Biot coefficient (t=20).

pose marginal effect on fracture propagation and cannot completely exploit the effect of natural fractures to form fracture networks. Thus, the injection rate should not be exceedingly high, and an adequately low injection rate with long fracturing cycle is more conducive toward the formation of a complex fracture network.

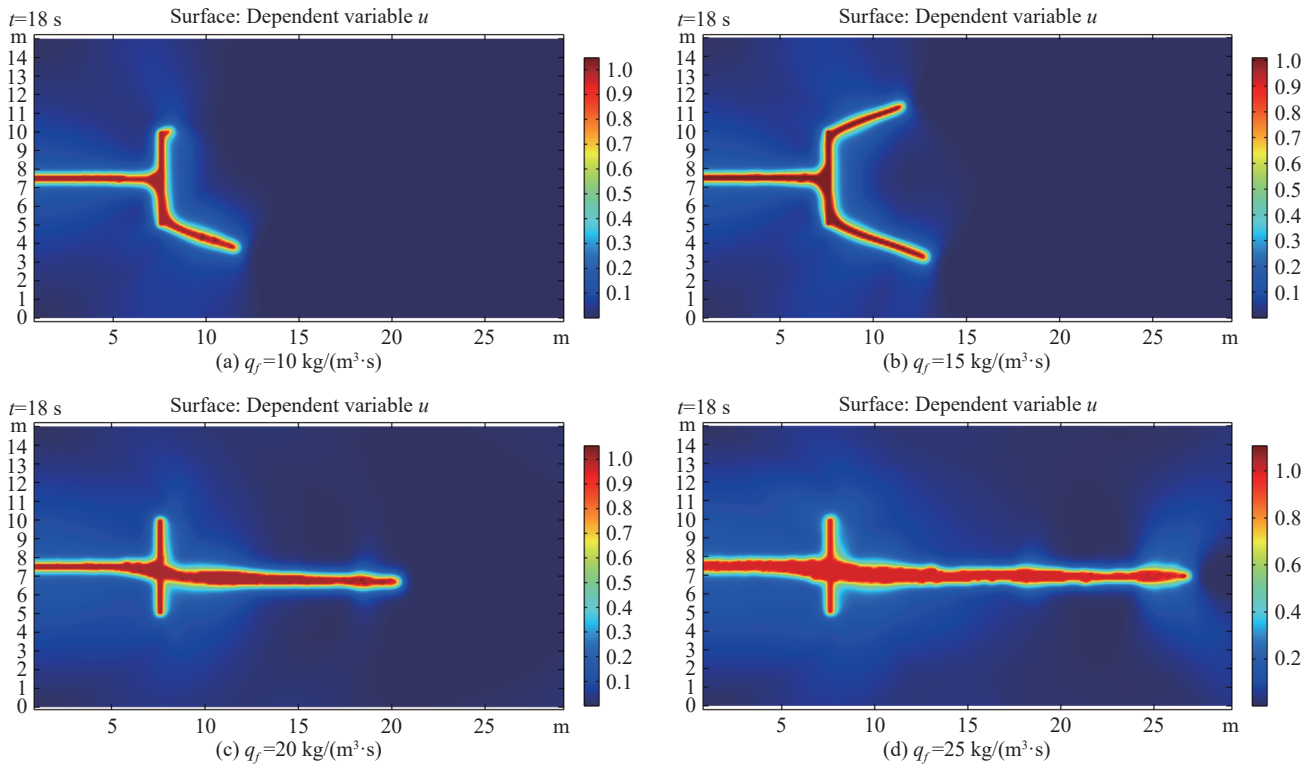

Fig. 18. Hydraulic fracture propagation pattern at different injection rates.

4.4. Stress distribution

Hot dry rock resource development typically occurs underground in formations spanning kilometers. In addition to temperature, groundwater, and rock mass defects, the presence of earth stress notably influences practical engineering in underground environments. In homogeneous media, hydraulic fractures tend to propagate along the plane of least compressive stress (Fu P et al., 2013). Nevertheless, in practical engineering, certain natural fractures will exist in the reservoir, and the stratigraphic conditions are considered heterogeneous. Thus, the study investigated the effect of stress distribution on fracture propagation in the presence of natural fractures by employing a control variable method. Overall, the angle between the injection unit and natural fracture (45°) did not vary, and the stress difference can be expressed as follows: (1) $\sigma_{x0}/\sigma_{y0} = 1$; (2) $\sigma_{x0}/\sigma_{y0} = 2$; (3) $\sigma_{x0}/\sigma_{y0} = 3$, where the minimum stress $\sigma_1 = 10$ MPa. The simulation results are depicted in Fig. 19 (fracture aperture is 1000-fold). For $\sigma_{x0} = \sigma_{y0}$, the hydraulic fracture propagated along the direction of the natural fracture after intersecting a natural fracture. In contrast, as the value of σ_{x0}/σ_{y0} increased, the propagation direction of the hydraulic fracture was influenced by the stress variations after fluid injection, extending along the direction of the large principal stress. This finding signified the dominant effect of stress distribution on the final direction of the artificial fracture if the value of σ_{x0}/σ_{y0} increased. The effect of various stress ratios on the rock breakdown pressure and rock damage ratio is presented in Fig. 20. As the stress ratio σ_{x0}/σ_{y0} increased, the rock breakdown pressure also increased.

4.5. Effect of fracture angle

The hydraulic fracturing process involves initiation, propagation, and penetration of rock microfractures under fluid pressure until the final macroscopic fracture is formed (Yang TH et al., 2002). In particular, the perforation hole forms the communication channel between the wellbore and formation. Most hydraulic fracturing operations occur in the casing perforation wells. Possibly, the shear failure may occur after encountering a hydraulic fracture at an angle with the natural fracture, thereby affecting the extended evolution of the hydraulic fracture. Therefore, the influence of intersection angles on the fracture propagation of heterogeneous rocks and prediction of breakdown pressure require further investigation. To ascertain the impact of the intersection angle on fracture propagation, the study predominantly utilized the control variable method. Herein, four models were set with an intersection angle of 30°, 45°, 60°, and 90°. According to the numerical simulation results (Fig. 21), the fractures first originated at the tip of the artificial fracture. In response to the gradually increasing pore water pressure, the facture expands outward and encounters a natural fracture during the propagation, thereby causing it to propagate along natural fracture. Finally, the hydraulic fractures disintegrated through the tip of the natural fractures, and their direction gradually deflected toward the maximum principal stress. Typically, a higher intersection angle causes a more prominent deflection of the fracture, but regardless of the variations in the fracture angle, the artificial fracture continued to develop along the direction of the maximum principal stress after breaking through the natural fracture. This finding implies that the natural fracture influences the propagation direction of the

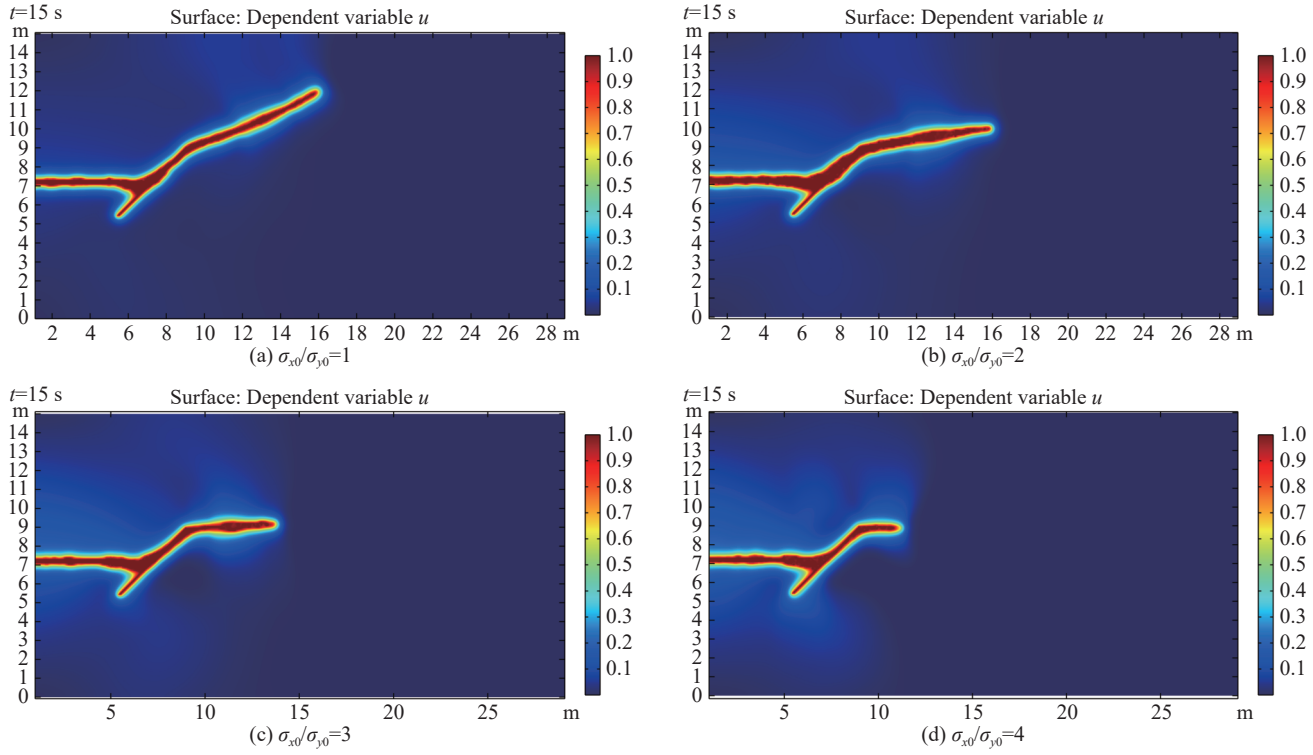

Fig. 19. Hydraulic fracture propagation of fluid injection under different stress states.

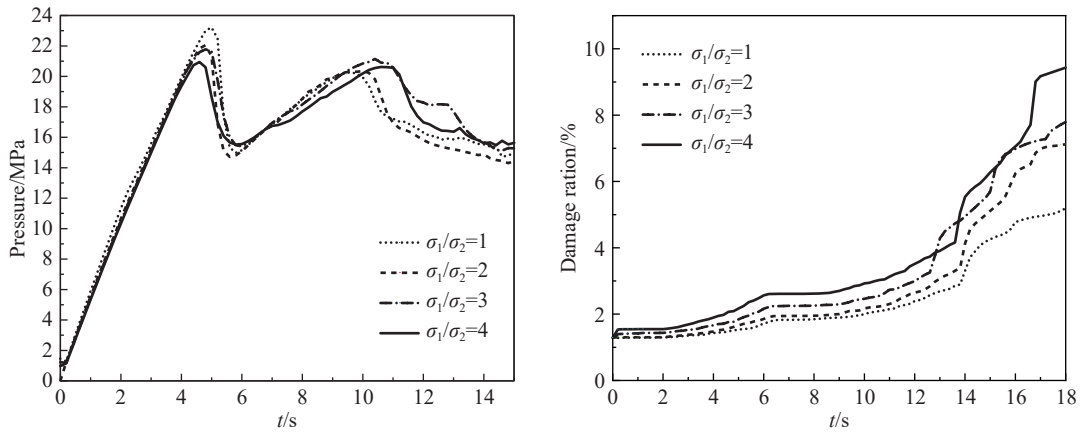

Fig. 20. Effect of σ_1/σ_2 ratio on fluid pressure and rock damage ration with time variation curve ($\theta = 45°$).

artificial fractures, but the maximum principal stress governs the final direction of fracture propagation. The variations in hydraulic pressure and damage ratio at various fracture angles are presented in Fig. 22. As the rock pressure was positively correlated with the intersection angle of the artificial and natural fractures and the rock breakdown pressure increased with the angle, the propagation of hydraulic fractures required more energy at larger angles.

4.6. Injection point position

The success of Enhanced Geothermal System (EGS) depends on establishing sustainable fluid channels between injection and production wells (Wang HW et al., 2022). Although the hydraulic stimulation does produce an extended fracture zone, the connection between the injection zone and the production zone is still a technically challenging. For example, Fenton Hill, Rosemanowes and Hijiori projects are facing connectivity problems in the early stages. These projects did not analyze the stimulated modification strips in advance, thus requiring some additional and costly drilling operations to achieve inter-well connectivity (Pollack A et al., 2020). Natural fractures are an important factor hindering inter-well connectivity, such as the Soultz project has poor connectivity between the wells due to vertical natural fractures (Genter A et al., 2010). To evaluate the effect of reservoir stimulation, numerical simulation is an effective method. According to Fig. 23, the NF (1) to NF (13) indicate naturally disconnected fractures, in which the NF (1) communicates with the boundary. To observe the effect of natural fractures on inter-well connectivity, fluid was injected into HF (1) and HF (2) to observe the fracture propagation direction. According to Fig. 23, the model size is 30 m×15 m. Fluid injection rates $q_f = 25\ \mathrm{kg}/\left(\mathrm{m}^3 \cdot \mathrm{s}\right)$ and the other

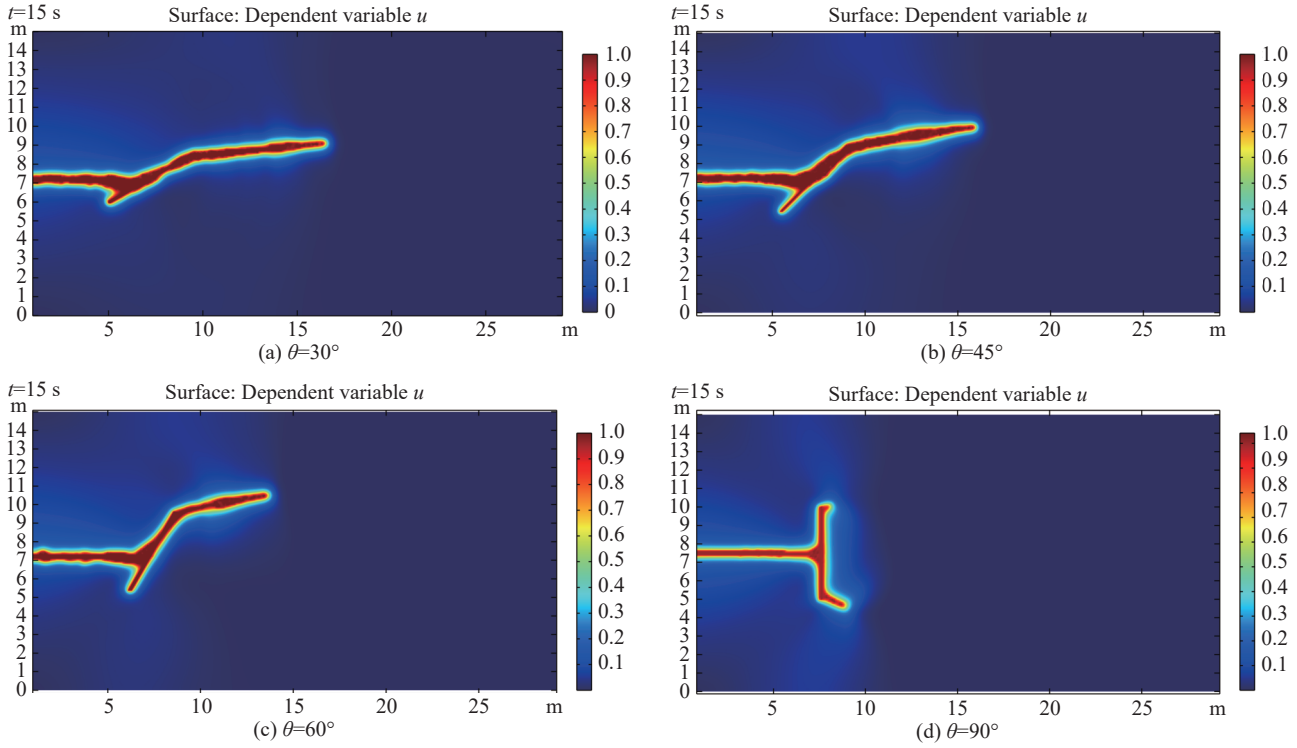

Fig. 21. Hydraulic fracture propagation at various fracture angles (fracture aperture is 1000-fold).

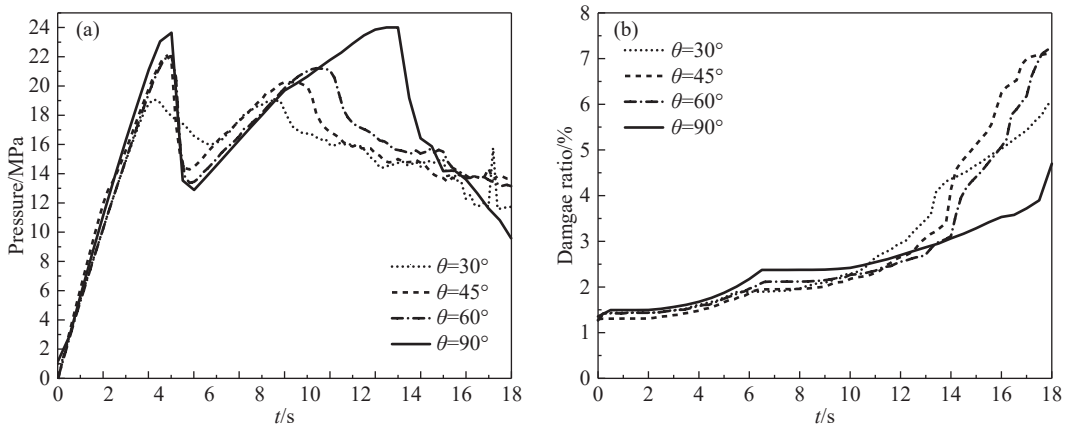

Fig. 22. Hydraulic pressure (a) and damage ratio (b) variation curve at different perforation angles.

parameters are shown in Table 2.

Fig. 24 shows the fracture propagation at different injection sites after 8 s. The HF propagation along the upper end of NF (2) to the upper end of NF (5) as the fluid is injected from HF (1). The flow path alters completely when fluid is injected from HF (2), first encountering NF (13) and propagating from the lower end of the fracture until it meets NF (10) and NF (1). It is not difficult to see that the trajectory of fracture propagation from HF (1) and HF (2) respectively cannot intersect, and once NF (1) is connected with other faults, there is a risk of fluid leakage. Thus, the rational use of natural fractures is EGS project important work because natural fractures are one of the important factors contributing to the disconnectivity between the wells.

4.7. Length of natural fracture

The fracture propagation influenced by natural fracture lengths of 2 m, 4 m, 6 m and 8 m is illustrated in Fig. 25 (fracture aperture is 1000-fold). Overall, a greater length of the natural fracture more significantly impacted the fracture initiation and propagation under hydraulic fracturing. For a natural fracture of 2 m length, the hydraulic fracture propagated in the direction of the maximum principal stress after intersection and the direction of the hydraulic fracture was less affected by the natural fracture. If the natural fracture exceeds 4 m in length, the path of the hydraulic fracture propagation will be significantly deflected after opening and penetrating through the natural fracture. However, its final propagation direction will be governed by the maximum horizontal stress, wherein a greater length of the natural fracture indicates a more prominent deflection. It is worth mentioning that the length of the natural fracture posed marginal influence on the breakdown pressure. However, as the fracture length increased, the hydraulic fracture required

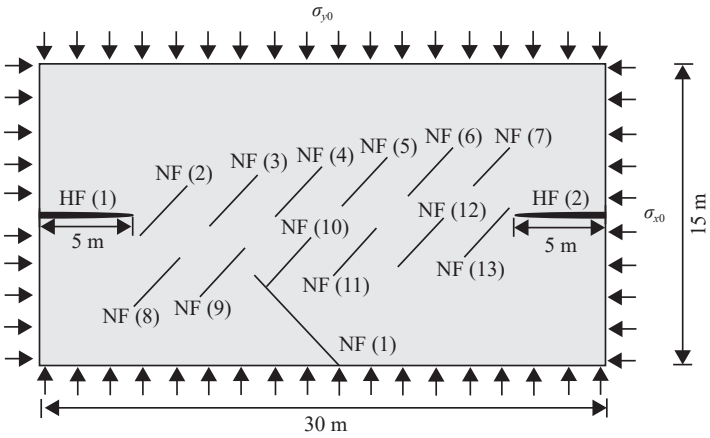

Fig. 23. Fracture geometries diagram.

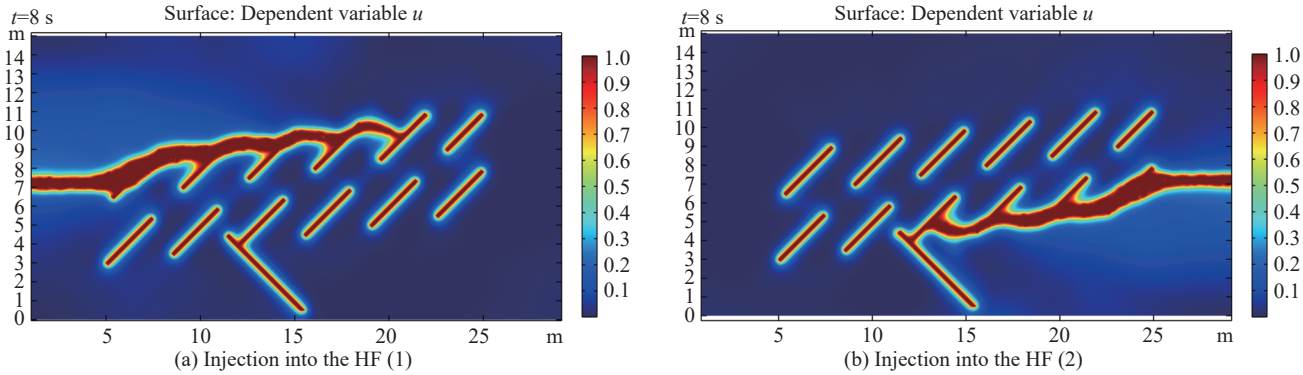

Fig. 24. Fracture propagation at different injection sites.

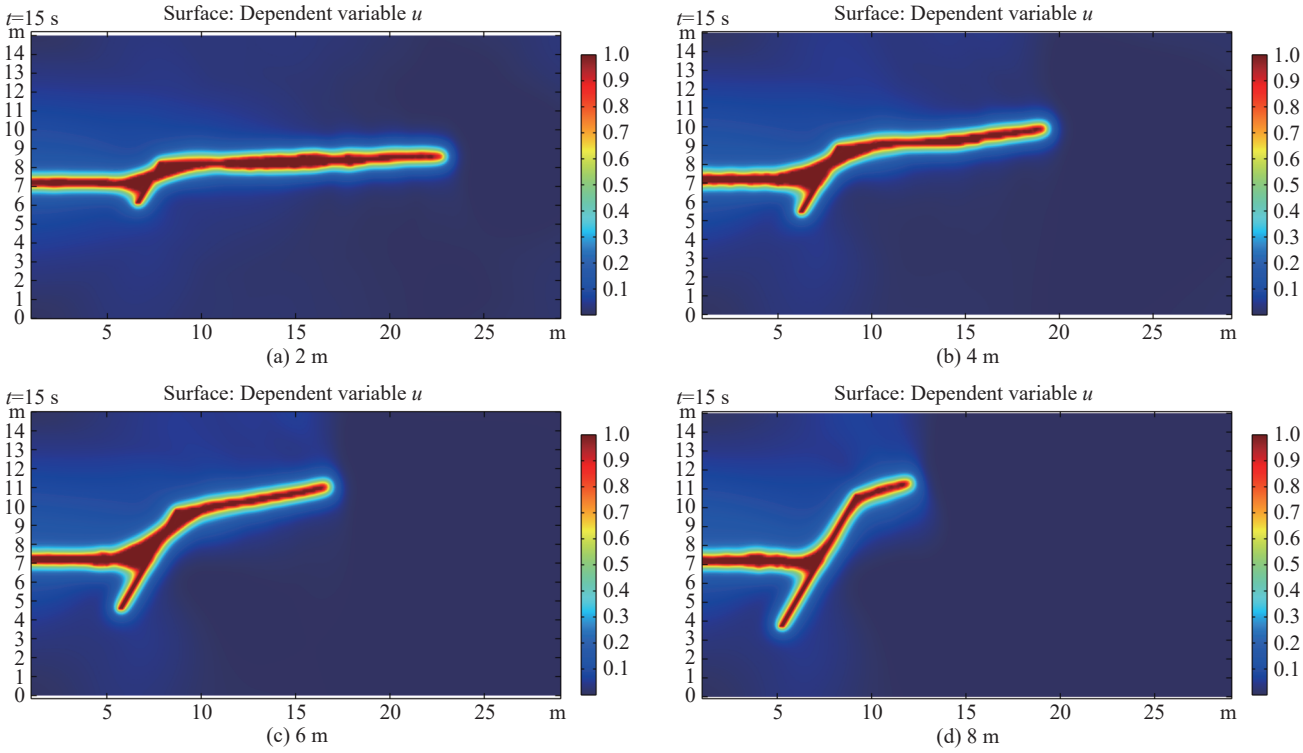

Fig. 25. Effect of natural fracture length on fracture propagation.

more fluid to propagate through the natural fracture. The propagation of the hydraulic fractures in presence of multiple disconnected natural fractures is presented in Fig. 26 (fracture aperture is 1000-fold). The results revealed that longer

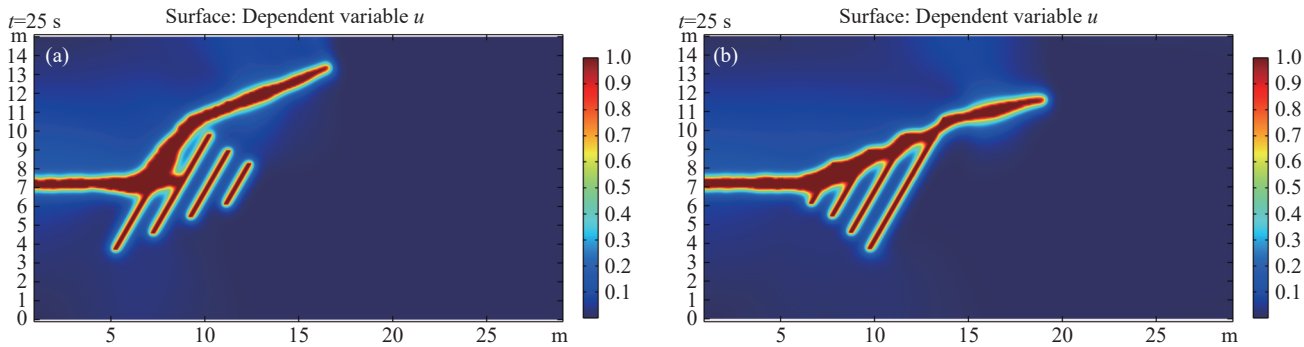

Fig. 26. Propagation of hydraulic fractures under multiple unconnected fractures.

fractures dominate path of the hydraulic fracture propagation. As such, these isolated long fractures restrict the area for heat exchange and cause a thermal short circuit if most of the injected fluid passes through it. At the Habanero project in Australia, the geothermal reservoir is considered a single, pre-existing fracture zone in which most of the injected fluid during cycle testing will flow between the wells along the fault (Genter A et al., 2009). This significantly reduces the assessment value of the potential recoverable thermal energy at the site. Similarly, 70% of the flow of the GPK-3 well is controlled by a fault zone at the Soultz project (Wang HW et al., 2022). Therefore, the fracture propagation path during hydraulic stimulation should avoid the intersection with individual large faults to prevent fluid leakage and uncontrollable movements.

5. Fractures propagating under complex fracture network

Based on prior numerical analyses, the influence of individual natural fractures on hydraulic fracture propagation has been established. However, an actual HDR reservoir typically contains multiple natural fractures. Consequently, it is imperative to simulate hydraulic fracture propagation within multifissured rock masses.

The impact of complex fracture networks on fracture propagation was explored using a two-dimensional discrete fracture network model of underground fracture rock mass. The model diagram is illustrated in Fig. 27, and the mechanical parameters of the material are listed in Table 2, wherein $q_f = 10\ \mathrm{kg/(m^3 \cdot s)}$, stress state of $\sigma_{x0} = 20$ MPa, and $\sigma_{y0} = 10$ MPa.

The simulated results exhibited that as the injection increased, the hydraulic fracture intersected the complex fractures, which opened and dilated the pre-fractures. Subsequently, the hydraulic fractures were distributed forward toward the weak plane tip or the fracture intersection prior to the fracture, which formed a dominant channel. Finally, the propagation of the fractures along the direction of maximum horizontal stress was caused by far-field stress after breaking through the fracture network. As depicted in Fig. 28 (fracture aperture is 1000-fold), all steering behaviors occurred at the weak plane tip or the fracture intersection. In addition, after the formation of the primary fluid channel in a natural fracture, the fluid cannot easily propagate in other fractures.

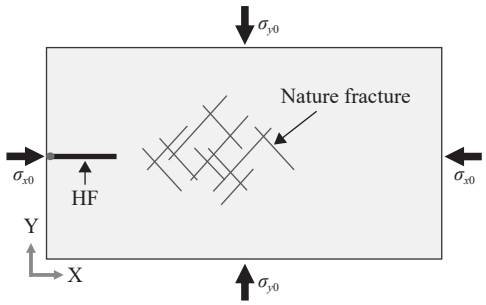

Fig. 27. Geometric model of complex fractures.

6. Conclusions

This research integrates Biot's poroelastic theory, seepage mechanics, and the phase field method to develop an extended transient phase field model for porous media. This model comprehensively considers the influence of the initial stress field and the complex natural fracture on the propagation of the hydraulic fracture. The main conclusions are as follows:

(i) When $\sigma_{x0}/\sigma_{y0} = 1$, the hydraulic fracture propagation direction is significantly altered by the natural fractures, while at $\sigma_{x0}/\sigma_{y0} \geqslant 3$, the hydraulic fracture continues to extend along the direction parallel to the maximum principal stress, after breaking through the natural fracture tip. Similarly, when the source term $q_f < 20\ \mathrm{kg/(m^3 \cdot s)}$, the hydraulic fracture propagates along the natural fracture, while $q_f \geqslant 20\ \mathrm{kg/(m^3 \cdot s)}$, it directly crosses the natural fracture. Thus, long-term, lower injection rates can form complex fracture networks in regions of low stress ratios. Conversely, the formation of the dominant channel can be reduced by controlling the wells and the orientation of the maximum principal in higher stress ratios area.

(ii) The breakdown pressure of the rock at $\theta = 90°$ is significantly higher than that at $\theta = 30°$. Considering the energy and heat transfer area, the optimal intersection angle for enhancing fracturing efficiency between natural fractures and hydraulic fractures ranges from 45° to 60°.

(iii) When the hydraulic fracutres encounter complex natural fractures, once the dominant channel is formed, the fluid will be difficult to expand in other directions. The length of the natural fracture is directly proportional to its influence on the hydraulic fracture. Additionally, it was also observed that the rock breakdown pressure at α = 0.1 is significantly

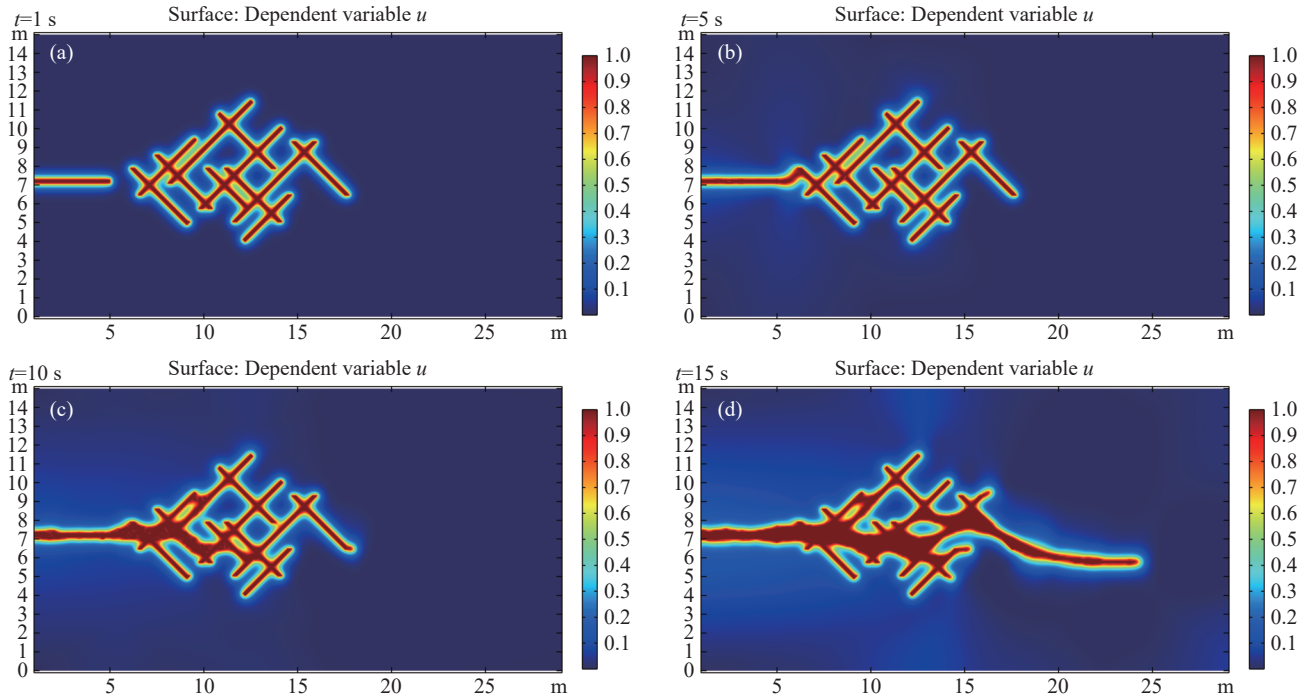

Fig. 28. Hydraulic fracture propagation path under complex fracture networks.

higher than at α = 0.5.

CRediT authorship contribution statement

Hong-wei Wang contributed to conceptualization, methodology, software development and writing the draft. Hai-dong Wu contributed to visualization and investigation. He-juan Liu and Yong-bo Tie contributed to methodology and software development. Li-sha Hu, Lin-you Zhang and Xian-peng Jin contributed to writing-review and editing.

Declaration of competing interest

The authors declare no conflicts of interest.

Acknowledgements

This research was supported by the National Key Research and Development Program (2021YFB150740401), National Natural Science Foundation of China (42202336) and the CAS Pioneer Hundred Talents Program in China (Y826031C01). The authors thank the reviewers who participated in the manuscript review.

References

Ambati M, Gerasimov T, De Lorenzis L. 2015. A review on phase-field models of brittle fracture and a new fast hybrid formulation. Computational Mechanics, 55(2), 383–405. doi: 10.1007/s00466-014-1109-y.

Areias P, Reinoso J, Camanho PP, César de Sá J, Rabczuk T. 2018. Effective 2D and 3D crack propagation with local mesh refinement and the screened Poisson equation. Engineering Fracture Mechanics, 189, 339–360. doi: 10.1016/j.engfracmech.2017.11.017.

Belytschko T, Lin JI. 1987. A three-dimensional impact-penetration algorithm with erosion. International Journal of Impact Engineering, 5(1–4), 111–127. doi: 10.1016/0734-743X(87)90033-9.

Biot MA. 1941. General theory of three-dimensional consolidation. Journal of Applied Physics, 12(2), 155–164. doi: 10.1063/1.1712886.

Borden MJ, Verhoosel CV, Scott MA, Hughes TJ, Landis CM. 2012. A phase-field description of dynamic brittle fracture. Computer Methods in Applied Mechanics and Engineering, 217, 77–95. doi: 10.1016/j.cma.2012.01.008.

Bourdin B, Francfort GA, Marigo JJ. 2008. The variational approach to fracture. Journal of Elasticity, 91(1), 5–148. doi: 10.1007/s10659-007-9107-3.

Bourdin B, Francfort GA, Marigo JJ. 2000. Numerical experiments in revisited brittle fracture. Journal of the Mechanics and Physics of Solids, 48(4), 797–826. doi: 10.1016/s0022-5096(99)00028-9.

Brown D, DuTeaux R, Kruger P, Swenson D, Yamaguchi T. 1999. Fluid circulation and heat extraction from engineered geothermal reservoirs. Geothermics, 28(4–5), 553–572. doi: 10.1016/S0375-6505(99)00028-0.

Chau-Dinh T, Zi G, Lee PS, Rabczuk T, Song JH. 2012. Phantom-node method for shell models with arbitrary cracks. Computers & Structures, 92, 242–256. doi: 10.1016/j.compstruc.2011.10.021.

Chen L, Rabczuk T, Bordas SPA, Liu GR, Zeng KY, Kerfriden P. 2012. Extended finite element method with edge-based strain smoothing (ESm-XFEM) for linear elastic crack growth. Computer Methods in Applied Mechanics and Engineering, 209, 250–265. doi: 10.1016/j.cma.2011.08.013.

Choo LQ, Zhao ZY, Chen HM, Tian Q. 2016. Hydraulic fracturing modeling using the discontinuous deformation analysis (DDA) method. Computers and Geotechnics, 76, 12–22. doi: 10.1016/j.compgeo.2016.02.011.

Francfort GA, Marigo JJ. 1998. Revisiting brittle fracture as an energy minimization problem. Journal of the Mechanics and Physics of Solids, 46(8), 1319–1342. doi: 10.1016/S0022-5096(98)00034-9.

Fu PC, Johnson SM, Carrigan CR. 2013. An explicitly coupled hydro-geomechanical model for simulating hydraulic fracturing in arbitrary discrete fracture networks. International Journal for Numerical and Analytical Methods in Geomechanics, 37(14), 2278–2300. doi:

10.1002/nag.2135.

Gao Q, Cheng YF, Han SC, Yan CL, Jiang L. 2019. Numerical modeling of hydraulic fracture propagation behaviors influenced by pre-existing injection and production wells. Journal of Petroleum Science and Engineering, 172, 976–987. doi: 10.1016/j.petrol.2018.09.005.

Genter A, Fritsch D, Cuenot N, Baumgärtner J, Graff JJ. 2009. Overview of the current activities of the European EGS Soultz project: From exploration to electricity production. In Proceedings, thirty-fourth workshop on geothermal reservoir engineering. Stanford, CA: Stanford University.

Genter A, Evans K, Cuenot N, Fritsch D, Sanjuan B. 2010. Contribution of the exploration of deep crystalline fractured reservoir of Soultz to the knowledge of enhanced geothermal systems (EGS). Comptes Rendus Géoscience, 342(7–8), 502–516. doi: 10.1016/j.crte.2010.01.006.

Genter A, Cuenot N, Melchert B, Moeckes W, Ravier G, Sanjuan B, Sanjuan R, Scheiber J, Schill E, Schmittbuhl J. 2013. Main achievements from the multi-well EGS Soultz project during geothermal exploitation from 2010 and 2012. Proceedings of European Geothermal Congress 2013.

Jiao YY, Zhang HQ, Zhang XL, Li HB, Jiang QH. 2015. A two-dimensional coupled hydromechanical discontinuum model for simulating rock hydraulic fracturing. International Journal for Numerical and Analytical Methods in Geomechanics, 39(5), 457–481. doi: 10.1002/nag.2314.

Kumari WGP, Ranjith PG. 2019. Sustainable development of enhanced geothermal systems based on geotechnical research–A review. Earth-Science Reviews, 199, 102955. doi: 10.1016/j.earscirev.2019.102955.

Lecampion B. 2009. An extended finite element method for hydraulic fracture problems. Communications in Numerical Methods in Engineering, 25(2), 121–133. doi: 10.1002/cnm.1111.

Lee S, Wheeler MF, Wick T. 2016. Pressure and fluid-driven fracture propagation in porous media using an adaptive finite element phase field model. Computer Methods in Applied Mechanics and Engineering, 305, 111–132. doi: 10.1016/j.cma.2016.02.037.

Lei QH, Gholizadeh DN, Tsang CF. 2021. Modelling fluid injection-induced fracture activation, damage growth, seismicity occurrence and connectivity change in naturally fractured rocks. International Journal of Rock Mechanics and Mining Sciences, 138, 104598. doi: 10.1016/j.ijrmms.2020.104598.

Li KC, Zhou SW. 2019. Numerical investigation of multizone hydraulic fracture propagation in porous media: New insights from a phase field method. Journal of Natural Gas Science and Engineering, 66, 42–59. doi: 10.1016/j.jngse.2019.03.018.

Liu HJ, Hou ZM, Li XC, Wei N, Tan X, Were P. 2015. A preliminary site selection system for a CO_2-AGES project and its application in China. Environmental Earth Sciences, 73(11), 6855–6870. doi: 10.1007/s12665-015-4249-2.

Liu HJ, Ban SN, Bédard K, Giroux B. 2022. Characteristics of Precambrian basement intruded by Cretaceous geological intrusions in Monteregian Igneous Province and their impacts on regional thermal structure. Advances in Geo-Energy Research, 6(3), 206–220. doi: 10.46690/ager.2022.03.04.

Liu J, Liang X, Xue Y, Fu Y, Yao K, Dou FK. 2020. Investigation on crack initiation and propagation in hydraulic fracturing of bedded shale by hybrid phase-field modeling. Theoretical and Applied Fracture Mechanics, 108, 102651. doi: 10.1016/j.tafmec.2020.102651.

Mikelić A, Wheeler MF, Wick T. 2015. A quasi-static phase-field approach to pressurized fractures. Nonlinearity, 28(5), 1371–1399. doi: 10.1088/0951-7715/28/5/1371.

Miehe C, Hofacker M, Welschinger F. 2010. A phase field model for rate-independent crack propagation: Robust algorithmic implementation based on operator splits. Computer Methods in Applied Mechanics and Engineering, 199(45–48), 2765–2778. doi: 10.1016/j.cma.2010.04.011.

Miehe C, Mauthe S, Teichtmeister S. 2015. Minimization principles for the coupled problem of Darcy–Biot-type fluid transport in porous media linked to phase field modeling of fracture. Journal of the Mechanics and Physics of Solids, 82, 186–217. doi: 10.1016/j.jmps.2015.04.006.

Moës N, Belytschko T. 2002. Extended finite element method for cohesive crack growth. Engineering Fracture Mechanics, 69(7), 813–833. doi: 10.1016/S0013-7944(01)00128-X.

Mikelic A, Wheeler MF, Wick T. 2013. A phase field approach to the fluid filled fracture surrounded by a poroelastic medium. ICES report, 1315.

Nguyen O, Repetto E, Ortiz M, Radovitzky R. 2001. A cohesive model of fatigue crack growth. International Journal of Fracture, 110(4), 351–369. doi: 10.1023/A:1010839522926.

Peerlings RD, De Borst R, Brekelmans WD, De Vree JHP, Spee I. 1996. Some observations on localisation in non-local and gradient damage models. European Journal of Mechanics. A, Solids, 15,937–953.

Pollack A, Horne R, Mukerji T. 2020. What are the challenges in developing Enhanced Geothermal Systems (EGS)? Observations from 64 EGS Sites. Proceedings World Geothermal Congress 2020, Reykjavik, Iceland, April 26–May 2.

Rabczuk T, Gracie R, Song JH, Belytschko T. 2010a. Immersed particle method for fluid–structure interaction. International Journal for Numerical Methods in Engineering, 81(1), 48–71. doi: 10.1002/nme.2670.

Rabczuk T, Zi G, Bordas S, Nguyen-Xuan H. 2010b. A simple and robust three-dimensional cracking-particle method without enrichment. Computer Methods in Applied Mechanics and Engineering, 199(37–40), 2437–2455. doi: 10.1016/j.cma.2010.03.031.

Rabczuk T, Belytschko T. 2004. Cracking particles: A simplified meshfree method for arbitrary evolving cracks. International Journal for Numerical Methods in Engineering, 61(13), 2316–2343. doi: 10.1002/nme.1151.

Rabczuk T, Zi G, Gerstenberger A, Wall WA. 2008. A new crack tip element for the phantom-node method with arbitrary cohesive cracks. International Journal for Numerical Methods in Engineering, 75(5), 577–599. doi: 10.1002/nme.2273.

Santillán D, Juanes R, Cueto-Felgueroso L. 2017. Phase field model of fluid-driven fracture in elastic media: Immersed-fracture formulation and validation with analytical solutions. Journal of Geophysical Research: Solid Earth, 122(4), 2565–2589. doi: 10.1002/2016jb013572.

Shimizu H, Murata S, Ishida T. 2011. The distinct element analysis for hydraulic fracturing in hard rock considering fluid viscosity and particle size distribution. International Journal of Rock Mechanics and Mining Sciences, 48(5), 712–727. doi: 10.1016/j.ijrmms.2011.04.013.

Song JH, Areias PMA, Belytschko T. 2006. A method for dynamic crack and shear band propagation with phantom nodes. International Journal for Numerical Methods in Engineering, 67(6), 868–893. doi: 10.1002/nme.1652.

Shiozawa S, Lee S, Wheeler MF. 2019. The effect of stress boundary conditions on fluid-driven fracture propagation in porous media using a phase-field modeling approach. International Journal for Numerical and Analytical Methods in Geomechanics, 43(6), 1316–1340. doi: 10.1002/nag.2899.

Selvadurai APS, Suvorov AP. 2020. The influence of the pore shape on the bulk modulus and the Biot coefficient of fluid-saturated porous rocks. Scientific Reports, 10, 18959. doi: 10.1038/s41598-020-75979-6.

Selvadurai APS. 2021. On the poroelastic Biot coefficient for a granitic rock. Geosciences, 11(5), 219. doi: 10.3390/geosciences11050219.

Wang HW, Liu HJ, Chen DF, Wu HD, Jin XP. 2022. Thermal response of the fractured hot dry rocks with thermal-hydro-mechanical coupling effects. Geothermics, 104, 102464. doi: 10.1016/j.geothermics.2022.102464.

Wang HW, Jin XP, Liu HJ, Wu HD, Liu DL, Song YJ, Ban SN, Tong RC, Qiu XS, Chen DF. 2024. Numerical investigations on the damage evolution in hot dry rocks with natural fractures induced by hydraulic stimulation. Geothermics, 123, 103114. doi: 10.1016/j.geothermics.2024.103114.

Wheeler MF, Wick T, Wollner W. 2014. An augmented-Lagrangian method for the phase-field approach for pressurized fractures. Computer Methods in Applied Mechanics and Engineering, 271, 69–85. doi: 10.1016/j.cma.2013.12.005.

Yang TH, Tham LG, Tang CA, Leng XF, Li LC. 2002. Influence of heterogeneity on hydraulic fracturing in rocks. Chinese Journal of Geotechnical Engineering, 24(6), 724–728 (in Chinese with English abstract).

Yan XC, Zheng J, Luo HH, Zhang H, Sun W, Dou B, Chen Y. 2024. Numerical simulation of wellbore fracture extension in hot dry rock wells under cold shock effect. Drilling Engineering, 51(3), 94–103 (in Chinese with English abstract).

Yan CZ, Zheng H, Sun GH, Ge XR. 2016. Combined finite-discrete element method for simulation of hydraulic fracturing. Rock Mechanics and Rock Engineering, 49(4), 1389–1410. doi: 10.1007/s00603-015-0816-9.

Yang YT, Tang XH, Zheng H, Liu QS, Liu ZJ. 2018. Hydraulic fracturing modeling using the enriched numerical manifold method. Applied Mathematical Modelling, 53, 462–486. doi: 10.1016/j.apm.2017.09.024.

Zhang W, Wang HH, Weng W, Yao SQ, Shao MJ. 2024. The latest deployment of the U. S. Department of Energy's geothermal drilling technology R & D and innovative practices in the demonstration of hot dry rock development. Drilling Engineering, 51(3), 1–8 (in Chinese with English abstract).

Zhang EY, Wen DG, Wang GL, Yan WD, Wang WS, Ye CM, Li XF, Wang H, Tang XC, Weng W, Li K, Zhang CY, Liang MX, Luo HB, Hu HY, Zhang W, Zhang SQ, Jin XP, Wu HD, Zhang LY, Feng QD, Xie JY, Wang D, He YC, Wang YW, Chen ZB, Cheng ZP, Luo WF, Yang Y, Zhang H, Zha EL, Gong YL, Zheng Y, Jiang CS, Zhang SS, Niu X, Zhang H, Hu LS, Zhu GL, Xu WH, Niu ZX, Yang L. 2022. The first power generation test of hot dry rock resources exploration and production demonstration project in the Gonghe Basin, Qinghai Province, China. China Geology, 5(3), 372–382. doi: 10.31035/cg2022038.

Zhou SW, Zhuang XY. 2018a. Adaptive phase field simulation of quasi-static crack propagation in rocks. Underground Space, 3(3), 190–205. doi: 10.1016/j.undsp.2018.04.006.

Zhou SW, Zhuang XY, Rabczuk T. 2018b. A phase-field modeling approach of fracture propagation in poroelastic media. Engineering Geology, 240, 189–203. doi: 10.1016/j.enggeo.2018.04.008.

Zhou SW, Rabczuk T, Zhuang XY. 2018c. Phase field modeling of quasi-static and dynamic crack propagation: COMSOL implementation and case studies. Advances in Engineering Software, 122, 31–49. doi: 10.1016/j.advengsoft.2018.03.012.

Zhou SW, Zhuang XY, Rabczuk T. 2019. Phase-field modeling of fluid-driven dynamic cracking in porous media. Computer Methods in Applied Mechanics and Engineering, 350, 169–198. doi: 10.1016/j.cma.2019.03.001.

Zhou SW, Zhuang XY, Rabczuk T. 2020a. Phase field method for quasi-static hydro-fracture in porous media under stress boundary condition considering the effect of initial stress field. Theoretical and Applied Fracture Mechanics, 107, 102523. doi: 10.1016/j.tafmec.2020.102523.

Zhou SW, Zhuang XY. 2020b. Phase field modeling of hydraulic fracture propagation in transversely isotropic poroelastic media. Acta Geotechnica, 15(9), 2599–2618. doi: 10.1007/s11440-020-00913-z.

Zhuang X, Zhou S, Huynh GD, Areias P, Rabczuk T. 2022. Phase field modeling and computer implementation: A review. Engineering Fracture Mechanics, 262, 108234. doi: 10.1016/j.engfracmech.2022.108234.

Zhou F, Molinari JF. 2004. Dynamic crack propagation with cohesive elements: A methodology to address mesh dependency. International Journal for Numerical Methods in Engineering, 59(1), 1–24. doi: 10.1002/nme.857.

Zhuang XY, Zhou SW, Sheng M, Li GS. 2020. On the hydraulic fracturing in naturally-layered porous media using the phase field method. Engineering Geology, 266, 105306. doi: 10.1016/j.enggeo.2019.105306.